Texture and composition of pumices and scoriae from the Campi Flegrei caldera (Italy): Implications on the dynamics of explosive eruptions

M. Piochi
Osservatorio Vesuviano, Istituto Nazionale di Geofisica e Vulcanologia, Via Diocleziano 328, I–80124 Naples, Italy (monky5@ov.ingv.it)

M. Polacci
Istituto Nazionale di Geofisica e Vulcanologia, Piazza Roma 2, I–95123 Catania, Italy

G. De Astis
Osservatorio Vesuviano, Istituto Nazionale di Geofisica e Vulcanologia, Via Diocleziano 328, I–80124 Naples, Italy

A. Zanetti
Istituto di Geoscienze e Georisorse, Consiglio Nazionale delle Ricerche, Via Ferrata 1, I–27100 Pavia, Italy

A. Mangiacapra
Osservatorio Vesuviano, Istituto Nazionale di Geofisica e Vulcanologia, Via Diocleziano 328, I–80124 Naples, Italy

R. Vannucci
Istituto di Geoscienze e Georisorse, Consiglio Nazionale delle Ricerche, Via Ferrata 1, I–27100 Pavia, Italy

Dipartimento di Scienze della Terra, Universitàdegli Studi di Pavia, Via Ferrata 1, I–27100 Pavia, Italy

D. Giordano
Dipartimento di Scienze Geologiche, Università degli Studi di Roma Tre, Largo San Leonardo Murialdo 1, I–00154 Rome, Italy

[1] The Campi Flegrei (CF) caldera is one of the most dangerous quiescent volcanic systems in the world. Its activity mostly resulted in low-magnitude explosive eruptions, such as that of the Monte Nuovo tuff cone that represents the last eruptive event within the caldera (A.D. 1538). However, there have been more energetic Plinian events, e.g., the Agnano Monte Spina eruption (4.1 ka), and very highly explosive, caldera-forming eruptions, e.g., the Campanian Ignimbrite eruption (39 ka). Here, we integrate new and literature data on the groundmass texture and composition of pyroclastic products from the three above eruptions with the aim of unraveling how volatiles content, degassing mechanisms, and crystallization processes influence magma explosivity and eruption dynamics at CF. Previous studies indicate that the investigated rocks share similar major element bulk and phenocryst chemistry; also similar is the water content of their trapped melt inclusions. These observations suggest that the magmas feeding these eruptions had comparable physicochemical properties during storage in the shallow crust. However, our investigations indicate that the studied rocks differ in texture and composition of the groundmass and viscosity of the related magmas. We ascribe such differences to the variable style of volatile exsolution and outgassing from the melt, primarily in response to changes of the rate of magma ascent to the surface. We conclude that the magma ascent rate was the key parameter in driving explosive eruptions at CF, and we

suggest that this parameter may be influenced by magma-water interaction and/or magma chamber geometry and replenishment.

1. Introduction

[2] Campi Flegrei (CF) has been the site of volcanic activity at least since the last 60 kyr B.P. (see *Piochi et al.* [2005a] for a review). In the past 15 ka, more than 60 eruptive vents opened in an area now occupied by the western town of Napoli, producing pyroclastic deposits that affected the region presently inhabited by 1.5 million people (Figure 1) [*Di Vito et al.*, 1999]. The last CF eruption occurred at Monte Nuovo in A.D. 1538 after about 3,000 years of quiescence [*Lirer et al.*, 1987].

[3] At present, intense hydrothermal activity, huge gas emissions with more than 1500 tons per day of CO_2 [*Chiodini et al.*, 2001] and bradyseisms [*Issel*, 1883] with an uplift up to 3.5 m in the last 30 years (see *Orsi et al.* [1999] for a review) provide evidence that the magmatic system is still active and the volcanic risk at CF is high [*Barberi et al.*, 1984]. As a consequence, numerous investigations are currently promoted and conducted by national and international research teams and networks to understand the dynamics of this volcanic area, to define the eruptive scenarios, to monitor its present state, to forecast its future evolution and, finally, to mitigate the overall volcanic risk.

[4] In the last decade, a huge effort has been devoted to highlight the link between syneruptive magmatic processes with the dynamics, intensity and magnitude of CF eruptions. Combined geochemical and textural studies on products from the Monte Nuovo tuff cone have shown the occurrence of syneruptive decompression-driven crystallization and volatile exsolution [*Piochi et al.*, 2005b; *D'Oriano et al.*, 2005]. Furthermore, textural studies on vesicles within juvenile products from

selected CF Plinian eruptions have been used to investigate conduit processes [*Polacci et al.*, 2003; *Polacci*, 2005] and constrain the numerical modeling of magma ascent along the conduit [*Polacci et al.*, 2004] considering the presence of CO_2 in addition to H_2O [*Esposti Ongaro et al.*, 2006].

[5] Here, we focus on the complex interplay between magma volatile composition, degassing and crystallization in driving CF explosive volcanism. In order to achieve this goal, we integrate literature data with a new data set on groundmass textures and compositions of pyroclastic products from three CF eruptions, namely the Campanian Ignimbrite (CI), Agnano Monte Spina (AMS) and Monte Nuovo (MTN) eruptions. These events cover a broad range of eruptive style, intensity and magnitude, while sharing similar petrochemical characteristics with a common trachytic composition. In addition, a proper characterization of the main rheological properties of their magmas [*Giordano et al.*, 2004, 2008] and of pre-eruptive physicochemical conditions [e.g., *Signorelli et al.*, 2001; *Papale and Gresta*, 2006; A. Roach and M. Rutherford, Pre-eruption conditions and eruption model of trachytic AMS magmas, Phlegrean Fields, Italy, submitted to *Journal of Petrology*, 2007] are already available in the literature.

2. Volcanological Background

[6] CF is a complex volcanotectonic area located in southern Italy (see *Piochi et al.* [2005a] for a review) (Figure 1). Its tectonic setting is dominated by a double calderic structure [*Rosi and Sbrana*, 1987; *Orsi et al.*, 1996, and references therein] generated during two very high magnitude, distinct explosive eruptions at 39 and 14.9 kyr B.P. [*De Vivo et al.*, 2001; *Deino et al.*, 2004].
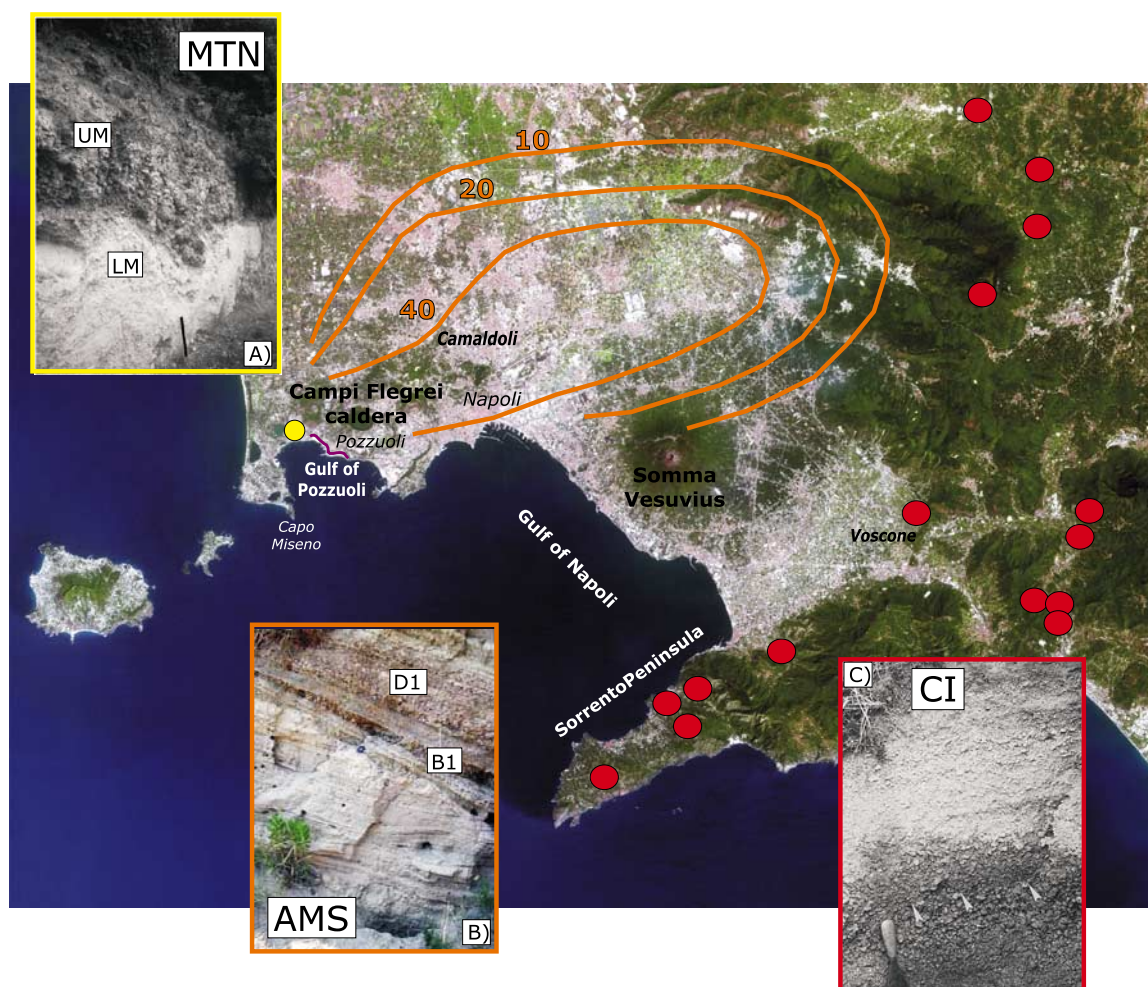
Figure 1. Active volcanic area of the Campanian region from a Landsat 7 satellite image (from the Laboratorio di Geomatica e Cartografia, Istituto Nazionale di Geofisica e Vulcanologia, Osservatorio Vesuviano, Napoli, Italy). The yellow dot locates the MTN cone. Red dots indicate outcrop location of the CI Plinian fallout. Orange lines define the areal distribution of the total fallout deposits (numbers are thickness values in centimeters) of the AMS eruption (modified from *de Vita et al.* [1999]). Magenta line identifies the La Starza terrace, generated by the volcanic-tectonic activity of the last 5 ka [see *Orsi et al.*, 1999]. Voscone and Camaldoli are locations of the sampled CI and AMS deposits. Details on the outcrop location are given in Table B1 (see Appendix B). (a) Photo of the MTN LM pumice and UM scoria units [from *D'Oriano et al.*, 2005]. (b) Photo of the AMS stratigraphic sequence (from the database of the Istituto Nazionale di Geofisica e Vulcanologia, Osservatorio Vesuviano, Napoli, Italy). (c) Photo of the CI Plinian fallout deposit [from *Rosi et al.*, 1999].

[7] The 39 ka event corresponds to the CI eruption, the largest magnitude explosive event of the Mediterranean area over the past 200 ka. It affected an area of about 7,000 km^2 and produced >150 km^3 Dense Rock Equivalent (DRE) of magma [*Fisher et al.*, 1993]. The CI volcanic succession includes a basal Plinian fallout and mostly welded ash and pumice flow deposits derived from several pyroclastic density currents generated through multiple feeding fractures (Figure 1). The Plinian fallout, with an estimated volume of 15 km^3 DRE, dispersed eastward and crops out beyond the Sorrento Peninsula [*Rosi et al.*, 1999].

[8] However, the majority of CF volcanic activity had a lower magnitude and intensity. In particular, the eruptions in the last 14.9 ka preferentially generated monogenetic scoria and tuff cones that localized within the caldera [*Rosi and Sbrana*, 1987; *Di Vito et al.*, 1999]. The typical volume of pyroclastic rocks produced during a single eruption is ~0.1 km^3 or less [*Lirer et al.*, 1987; *Rosi and Sbrana*, 1987; *Di Vito et al.*, 1999, and references therein].

[9] The AMS eruption (4.1 ka) is the largest among those younger than 14.9 ka and is considered as a reference episode for the maximum expected event in a case of CF unrest [*Rosi and Santacroce*, 1984; *de Vita et al.*, 1999; *Dellino et al.*, 2001]. It produced a complex sequence of Plinian/sub-Plinian pumice fallout deposits alternating or contemporaneous with phreatomagmatic ash base-surge beds (Figure 1) [*de Vita et al.*, 1999]. The total volume of the deposits is 1.2 km^3 DRE, including 0.025 km^3 DRE of pumice fallout [*de Vita et al.*, 1999].

[10] The MTN eruption occurred in A.D. 1538 on the western edge of La Starza tectonic terrace (Figure 1). The MTN products, with a total volume of 10^7 m^3 DRE [*Lirer et al.*, 1987; *D'Oriano et al.*, 2005], are distributed between Capo Miseno and Pozzuoli, but they mostly crop out on the volcanic edifice itself. The stratigraphic sequence can be subdivided in two main units [*Di Vito et al.*, 1987; *D'Oriano et al.*, 2005]: (1) the Lowermost Member (hereafter LM), generated by phreatomagmatic and low-energy magmatic explosions, consists of yellowish, plane-parallel to wavy fine to coarse ash beds containing cm- to dm-sized fragments both dispersed and concentrated in layers or lenses; (2) the Uppermost Member (hereafter UM), generated by Vulcanian/Strombolian explosions, mostly includes grey to dark-colored coarse-grained scoria fragments and dense clasts.

[11] Most of the CF volcanic rocks show similar mineralogical and geochemical characteristics. These rocks are potassic and generally display nearly aphyric to slightly porphyritic textures (see *Piochi et al.* [2005a] for a review). The phenocrysts are dominantly K-feldspar, plagioclase, apatite and Fe-oxides, and subordinately clinopyroxene and biotite; olivine is rare [*Rosi and Sbrana*, 1987; *Civetta et al.*, 1997; *D'Antonio et al.*, 1999; *de Vita et al.*, 1999; *Signorelli et al.*, 2001]. Most commonly, whole rock chemistry displays trachytic to trachy-phonolitic compositions. Sr isotope data indicate that volcanism in the last 14.9 ka was fed by three main compositional end-members, referred to as the CI, NYT (Neapolitan Yellow Tuff) and MI (Minopoli) components; interesting-

ly, the CI and the NYT components have signatures similar to those of volcanic rocks produced during the two caldera-forming eruptions [*D'Antonio et al.*, 1999].

3. Sample Selection, Description, Preparation, and Analysis

[12] The CI, AMS, and MTN rocks, representing the product of eruptions with very high, high and low intensity and magnitude, respectively, have been selected for our purposes because they met the following requisites: (1) the availability of reliable information on the eruptive mechanisms and the plumbing system [*Lirer et al.*, 1987; *de Vita et al.*, 1999; *Rosi et al.*, 1999]; (2) the overall similarity of petrochemical characteristics to minimize pre-eruptive magma composition effects [*D'Antonio et al.*, 1999]; (3) the availability of previous textural information [*Polacci et al.*, 2003; *D'Oriano et al.*, 2005; *Piochi et al.*, 2005b; *Polacci*, 2005] and (4) the possibility to derive the rheological properties of the related magmas [*Giordano et al.*, 2004, 2008]. Furthermore, the AMS and MTN rocks were produced by eruptions relevant for their implications on volcanic hazard, being the most energetic and the most likely event in the case of unrest at CF [*Rosi and Santacroce*, 1984; *Dellino et al.*, 2001], respectively.

[13] The sampled rocks consist of trachytic pumice and scoria clasts. Pumice clasts have been sampled from (see Figure 1 for outcrop location and Table B1 (Appendix B) for details on sampled sites) (1) the CI basal Plinian fallout deposit cropping out at Voscone; (2) the AMS Plinian fallout (layers B1 and D1) cropping out at Camaldoli and (3) the base and the top of the LM from MTN. Scoria clasts have been collected from the UM base and the UM top of MTN.

[14] The juvenile fraction selected for our investigations is representative of the sampled deposits and show no evidence of alteration and post-fragmentation processes. Pumice clasts are mostly angular and yellow in color, corresponding to the microvesicular and tube pumice types described by *Polacci* [2005]. The great majority (up to 70%) of

Figure 2. Typical 2-D textures of yellow microvesicular and tube pumices from CI and AMS eruptions and of LM yellow microvesicular pumices, LM banded pumices, and UM scoriae from MTN explosions. The first photo in each set is a polarized light optical image, the second photo is a transmitted light optical image, and the third photo is a backscattered SEM image. Note that in the MTN banded pumice clast, the less vesicular and more crystallized area is highlighted by the red sign in the first and second photos and occurs in the top right zone of the third photo. Further details in the text.

Scoria from Monte Nuovo

Banded pumice from Monte Nuovo

Yellow microvesicular pumice from Monte Nuovo (LM inf)

Figure 2

Yellow tube pumice from Agnano Monte Spina

Yellow microvesicular pumice from Agnano Monte Spina

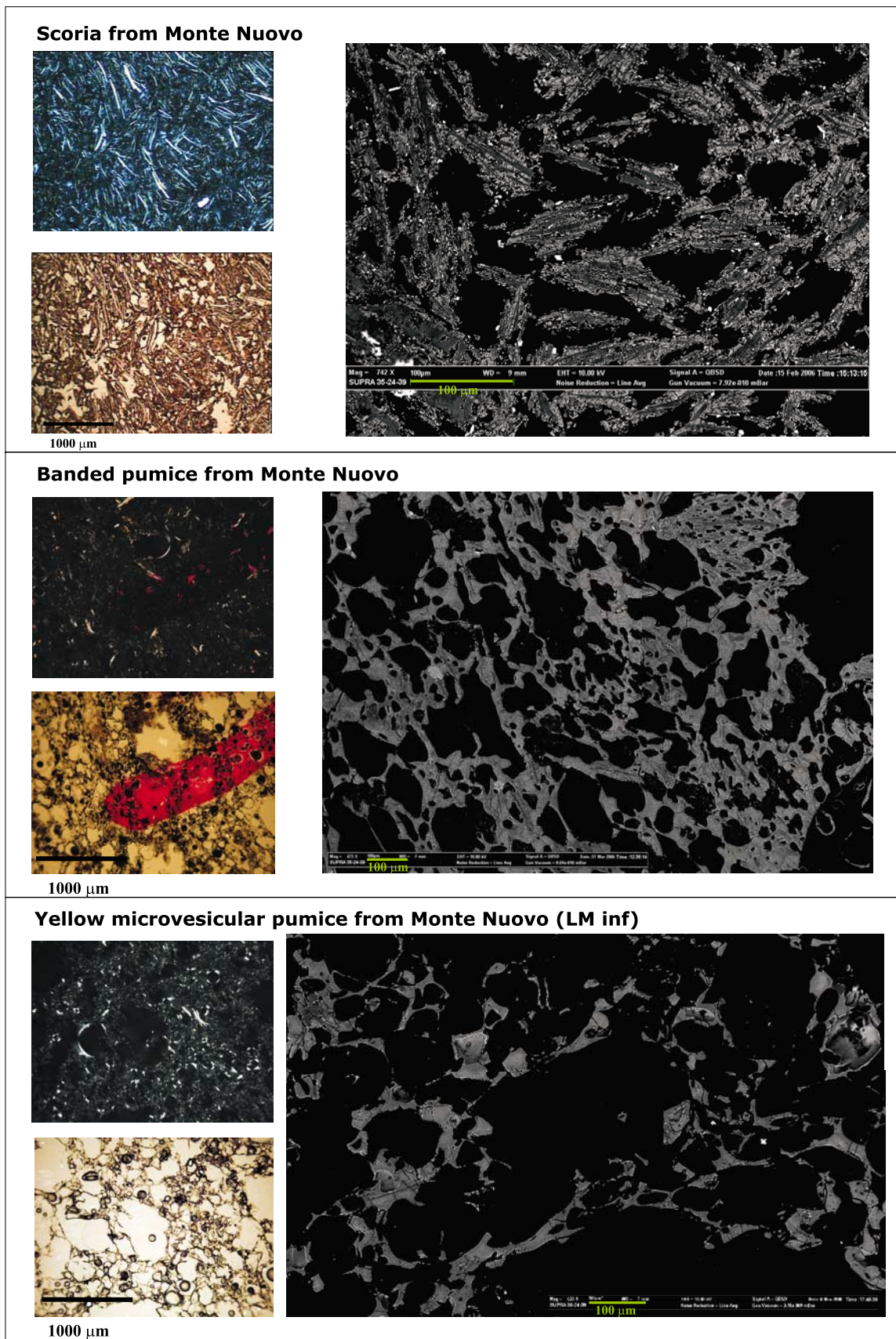
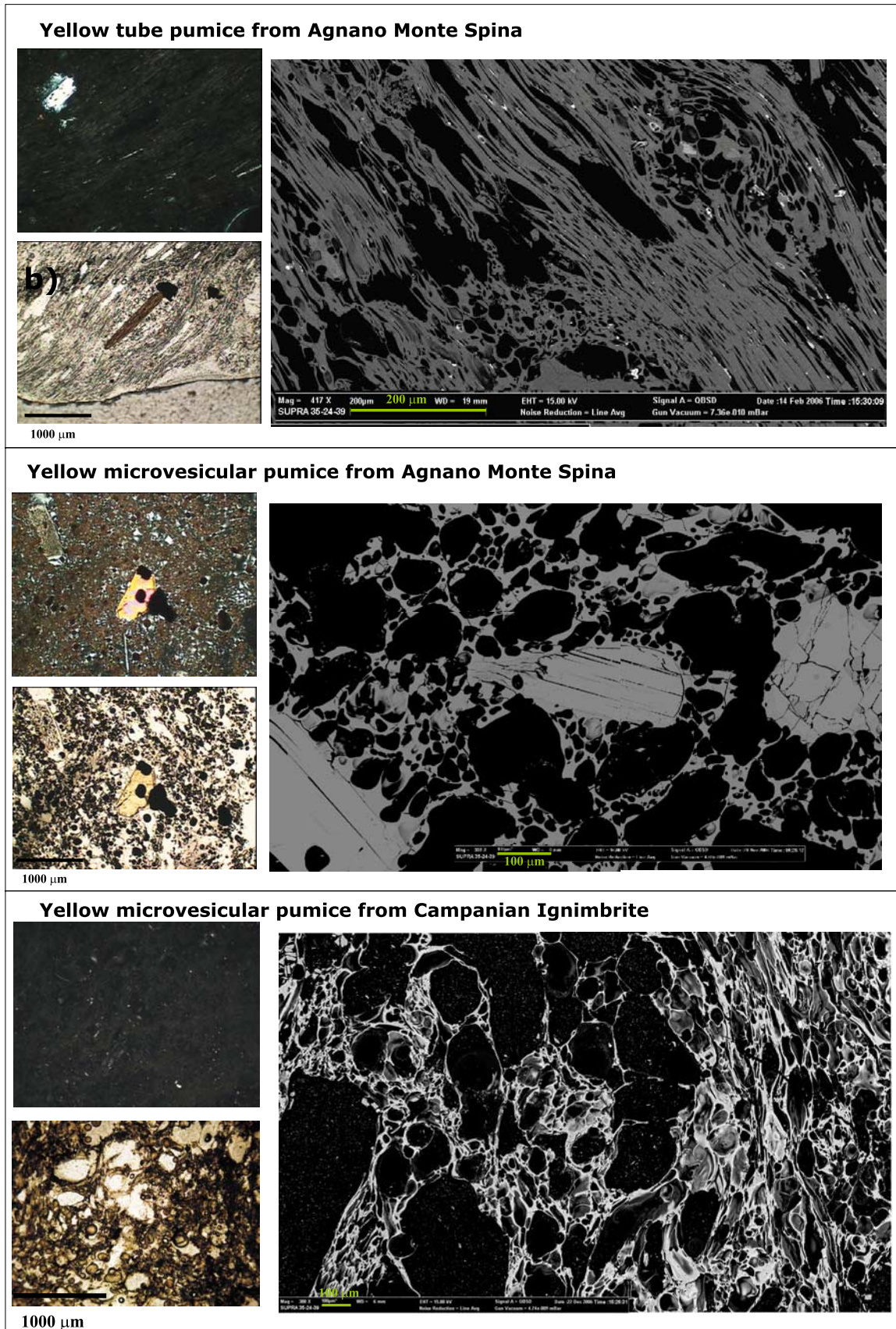**Yellow microvesicular pumice from Campanian Ignimbrite**

Figure 2. (continued)

juvenile clasts in the fallout deposits of AMS and CI consists of yellow microvesicular pumices [*Polacci et al.*, 2003; *Polacci*, 2005], which also occur in the LM of MTN. Yellow tube pumice clasts, characterized by flattened shapes and alignments of highly stretched, deformed vesicles, subordinately occur within the same stratigraphic layer. The LM of the MTN deposit also contains abundant banded pumices characterized by the alternation of yellow (more vesicular) and brown (less vesicular) portions, separated by sharp contacts. MTN banded pumices can be dominated by brown bands and are hereafter named brown pumices. Scoriae mostly consist of black clasts.

[15] Selected fragments were prepared for (1) qualitative and quantitative 2-D textural investigations; (2) in situ major and trace element analyses and (3) in situ and bulk measurements of the water content of the matrices (hereafter in situ residual water content and bulk residual water content, respectively). Details about the adopted analytical procedures are in Appendix A.

[16] Conventional, rectangular polished thin sections (typically 30 μm thick) were prepared for 2-D textural investigations by Optical and Scanning Electron Microscopy and for major element analysis of the glassy groundmass and microlites by Electron Microprobe. AMS yellow tube pumice clasts were cut along and orthogonal to the vesicle alignment. Round (1-inch in diameter) polished thin sections (60–80 μm thick) have been prepared for Electron, Laser and Ion Microprobe analyses to measure in situ major, trace and volatile contents of the glassy groundmass. Because our samples are highly vesicular and some of them exhibit heterogeneous volatile composition at the micron scale (see Table 4 and section 4.5), we prepared a phenocryst-free grain size fraction of selected AMS and MTN pumices and scoriae and measured the residual bulk-water content by means of a procedure commonly used in experimental petrology [see, e.g., *Di Matteo et al.*, 2004; *Giordano et al.*, 2004]. This procedure, described in Appendix A (section A5), allowed us to obtain homogeneous vesicle-free glasses representative of the phenocrysts-free magma at the eruptive conditions. Double-polished wafers of these synthesized glasses were then prepared and analyzed by FT-IR for the bulk H_2O and CO_2 content (see Appendix A for details).

[17] Finally, 3-D textural investigations have been performed on selected samples (namely, (1) three yellow microvesicular pumice clasts from the CI fall deposit; (2) two yellow microvesicular pumice clasts from the B1 fall layer of AMS and (3) two yellow microvesicular pumice and scoria clasts from both LM and UM of MTN), considered representative of the variability exhibited by the studied deposits. The clasts were cut into 2 cm high parallelepipeds (bottom and top surface ~25 mm²) and analyzed via Synchrotron X-ray Computed Microtomography (see Appendix A for details). One clast from each unit was processed for 3-D quantification of vesicle textures.

4. Results

4.1. Petrography

[18] The MTN, AMS and CI samples investigated here display variably vesicular and partially crystallized, unaltered glassy groundmasses (Figure 2). The CI and MTN juvenile fragments contain less than 5% of phenocrysts, mostly consisting of plagioclase and K-feldspar, and subordinate clinopyroxene. Sphene and amphibole phenocrysts occasionally occur in the MTN products. The AMS yellow microvesicular and tube pumice fragments contain up to 30% phenocrysts, which consist of K-feldspar, plagioclase, clinopyroxene, biotite and magnetite, in order of decreasing abundance. The observed phenocrysts are commonly euhedral, however, some phenocrysts with resorbed margins have been also described in products from AMS [*de Vita et al.*, 1999].

[19] The groundmass of CI yellow microvesicular pumices is exclusively glassy. Conversely, microlites occur in both MTN and AMS products, although the content is lower in the latter. MTN microlites are alkali-feldspar ranging in shape from tabular to acicular to dendritic; they frequently form radiating aggregates, and, rarely, spherulites. Scoria clasts with highly crystallized groundmasses may display microlites of magnetite (see Table 1). Generally, MTN microlite abundance and size increase from LM to UM products. Microlites are sometimes curved and follow the border of vesicles, reflecting the contemporaneous growth of vesicles and crystals. AMS microlites mostly consist of tabular to acicular plagioclase and clinopyroxene.

[20] In the yellow microvesicular pumices of CI, AMS and MTN, as well as in MTN banded pumices, vesicles may be either rounded or moderately elongated. However, in the studied MTN pumice types, elongation often results from vesicle coalescence (Figure 2). In the yellow microvesic-

Table 1. New 2-D Textural Data on Clasts From CI, AMS, and MTN Eruptions by Scanning Electron Microscopy[a]

Unit	Clast Type/Feature	Sample	Vesicles					Groundmass			Microlites		
			Analyzed Area, mm²	Area, mm²	N°	Vesicularity, %	Number Density, mm⁻²	Area, mm²	Area, mm²	N°	Microcrystallinity, %	Population Density, mm⁻²	Mt[b]
						Monte Nuovo							
LMinf	YM pumice[c]	LM inf1 01–07	0.761	0.630	143	83	1.9E + 02	0.131	0.003	37	2	2.8E + 02	n.d.
LMinf	YM pumice	LM inf2 08–11	0.510	0.406	433	80	8.5E + 02	0.104	0.000	15	0	1.4E + 02	n.d.
LMinf	*YM pumice*	*whole LMinf1*	*1.271*	*1.036*	*576*	*82*	*4.5E + 02*	*0.235*	*0.003*	*52*	*1*	*2.2E + 02*	*n.d.*
LMinf	*brown band*	*LMinbsc 02–05*	*0.719*	*0.430*	*221*	*60*	*3.1E + 02*	*0.289*	*0.034*	*621*	*12*	*2.2E + 03*	*n.d.*
LMinf	yellow band	LMinb 01–04	0.433	0.269	50	62	1.2E + 02	0.164	0.007	57	4	3.5E + 02	n.d.
LMinf	yellow band	LMinb ch 07–10	1.180	0.769	255	65	2.2E + 02	0.411	0.032	417	8	1.0E + 03	n.d.
LMinf	*yellow band*	*whole LMinb*	*1.613*	*1.038*	*305*	*64*	*1.9E + 02*	*0.575*	*0.039*	*474*	*7*	*8.2E + 02*	*n.d.*
LM	YM pumice	LM c1 01–07	0.703	0.551	317	78	4.5E + 02	0.152	0.002	14	1	9.2E + 01	*
LM	YM pumice	LM c1 08–13	0.776	0.504	645	65	8.3E + 02	0.272	0.014	282	5	1.0E + 03	*
LM	*YM pumice*	*whole LM c1*	*1.479*	*1.055*	*962*	*71*	*6.5E + 02*	*0.424*	*0.016*	*296*	*4*	*7.0E + 02*	***
LM	YM pumice	MN 2/2 01–03	0.289	0.207	183	72	6.3E + 02	0.082	0.005	84	6	1.0E + 03	n.d.
LM	YM pumice	MN 2/2 4	0.191	0.131	152	69	8.0E + 02	0.060	0.004	106	7	1.8E + 03	n.d.
LM	YM pumice	MN 2/2 06–09	0.693	0.483	374	70	5.4E + 02	0.210	0.035	331	17	1.6E + 03	n.d.
LM	*YM pumice*	*whole MN 2/2*	*1.173*	*0.821*	*709*	*70*	*6.0E + 02*	*0.352*	*0.044*	*521*	*12*	*1.5E + 03*	*n.d.*
LM	YM pumice	MN 2/1 08	0.201	0.146	95	73	4.7E + 02	0.055	0.014	109	25	2.0E + 03	**
LM	YM pumice	MN 2/1 09	0.059	0.030	137	51	2.3E + 03	0.029	0.008	285	27	9.8E + 03	**
LM	*YM pumice*	*whole MN 2/1*	*0.260*	*0.176*	*232*	*68*	*8.9E + 02*	*0.084*	*0.022*	*394*	*26*	*4.7E + 03*	***
LM	*yellow band*	*LM c2 c4–7*	*0.408*	*0.188*	*1383*	*46*	*3.4E + 03*	*0.220*	*0.041*	*980*	*19*	*4.5E + 03*	
LM	*brown band*	*LM c2 s9–12*	*0.459*	*0.165*	*343*	*36*	*7.5E + 02*	*0.294*	*0.064*	*1150*	*22*	*3.9E + 03*	*
LM	brown band	MN 1/1b 105a	0.201	0.073	401	36	2.0E + 03	0.128	0.024	593	19	4.6E + 03	n.d.
LM	brown band	MN 1/1b 107b	0.200	0.067	144	33	7.2E + 02	0.133	0.030	574	22	4.3E + 03	n.d.
LM	*brown band*	*whole MN 1/1b*	*0.401*	*0.140*	*545*	*35*	*1.4E + 03*	*0.261*	*0.054*	*1167*	*21*	*4.5E + 03*	*n.d.*
LM	brown band	MN 1/1c 12a	0.201	0.089	122	44	6.1E + 02	0.112	0.024	481	22	4.3E + 03	**
LM	brown band	MN 1/1c 13a	0.059	0.027	175	46	3.0E + 03	0.032	0.009	339	28	1.1E + 04	*
LM	*brown band*	*whole MN 1/1c*	*0.260*	*0.116*	*297*	*45*	*1.1E + 03*	*0.144*	*0.033*	*820*	*23*	*5.7E + 03*	***
LM	brown pumice	LM c3 01–07	0.574	0.260	1161	45	2.0E + 03	0.314	0.072	1978	23	6.3E + 03	n.d.
LM	banded pumice	MN 2/3 14a	0.266	0.157	115	59	4.3E + 02	0.109	0.017	241	16	2.2E + 03	**
LM	banded pumice	MN2/3 15a	0.070	0.040	53	57	7.5E + 02	0.030	0.005	156	16	5.1E + 03	**
LM	*banded pumice*	*whole MN 2/3*	*0.336*	*0.197*	*168*	*59*	*5.0E + 02*	*0.139*	*0.022*	*397*	*16*	*2.8E + 03*	***
LM	*black scoria*	*UM1 10–11*	*0.333*	*0.136*	*260*	*41*	*7.8E + 02*	*0.197*	*0.051*	*540*	*26*	*2.7E + 03*	***
UM1	black scoria	MN4 top 02–05	0.059	0.037	529	63	9.0E + 03	0.022	0.007	274	32	1.3E + 04	*****
UM1 top	black scoria	MN4 top 06–2	0.148	0.086	77	58	5.2E + 02	0.062	0.016	311	26	5.0E + 03	****
UM1 top	*black scoria*	*whole MN4top*	*0.206*	*0.123*	*606*	*60*	*2.9E + 03*	*0.083*	*0.023*	*585*	*28*	*7.0E + 03*	***
UM2	black scoria	MN 4/1 02a	0.283	0.137	307	48	1.1E + 03	0.146	0.045	303	31	2.1E + 03	***
UM2	black scoria	MN 4/1 04a	0.071	0.034	58	48	8.2E + 02	0.037	0.013	184	35	5.0E + 03	***
UM2	*black scoria*	*whole MN 4/1*	*0.354*	*0.171*	*365*	*48*	*1.0E + 03*	*0.183*	*0.058*	*487*	*32*	*2.7E + 03*	***

Table 1. (continued)

| Unit | Clast Type/Feature | Sample | Vesicles | | | | | Groundmass | Microlites | | | | |
			Analyzed Area, mm²	Area, mm²	N°	Vesicularity, %	Number Density, mm⁻²	Area, mm²	Area, mm²	N°	Microcrystallinity, %	Population Density, mm⁻²	Mt[b]
						Agnano Monte Spina							
Fallout B	YM pumice	AMS B1 02	1.864	1.467	541	79	2.9E + 02	0.397	0.007	5	2	1.3E + 01	n.d.
Fallout B	YM pumice	AMS B1 06	0.490	0.282	97	58	2.0E + 02	0.208	0.001	3	0	1.4E + 01	n.d.
Fallout B	YM pumice	AMS B1 05	0.104	0.081	68	78	6.5E + 02	0.023	-	-	-	-	n.d.
Fallout B	YM pumice	AMS B1 03	0.118	0.081	264	68	2.2E + 03	0.037	-	-	-	-	n.d.
Fallout B	*YM pumice*	*whole AMS B1*	*2.577*	*1.911*	*970*	*74*	*3.8E + 02*	*0.666*	*0.008*	*8*	*1*	*1.2E + 01*	*n.d.*
Fallout D1	YM pumice	AMS D1top 02–05	0.743	0.459	395	62	5.3E + 02	0.284	-	-	-	-	n.d.
Fallout D1	YM pumice	AMS D1top 06	1.934	1.388	402	72	2.1E + 02	0.546	-	-	-	-	n.d.
Fallout D1	YM pumice	AMS D1top 07	3.473	2.377	620	68	1.8E + 02	1.096	-	-	-	-	n.d.
Fallout D1	*YM pumice*	*whole AMS D1*	*6.150*	*4.224*	*1417*	*69*	*2.3E + 02*	*1.926*	*-*	*-*	*-*	*-*	*n.d.*
Tube	tube pumice	FL1c 01	0.689	0.211	1104	31	1.6E + 03	0.478	-	-	-	-	n.d.
Tube	tube pumice	FL1c 02	0.532	0.146	875	27	1.6E + 03	0.386	-	-	-	-	n.d.
Tube	tube pumice	FL1c 06 + 07	0.677	0.314	1898	46	2.8E + 03	0.363	0.001	-	0	-	n.d.
Tube	*tube pumice*	*whole FL1c*	*1.897*	*0.671*	*3877*	*35*	*2.0E + 03*	*1.226*	*-*	*-*	*-*	*-*	*n.d.*
Tube	tube pumice	FL1a 01–08	0.975	0.381	2950	39	3.0E + 03	0.594	0.002	8	0	1.3E + 01	n.d.
Tube	tube pumice	FL1a 11–14	0.864	0.350	2094	41	2.4E + 03	0.514	0.001	9	0	1.8E + 01	n.d.
Tube	*tube pumice*	*whole FL1a*	*1.839*	*0.731*	*5044*	*40*	*2.7E + 03*	*1.108*	*0.003*	*17*	*0*	*1.5E + 01*	*n.d.*
						Campanian Ignimbrite							
Fallout	YM pumice	IC60-90 08–14	2.549	1.720	850	67	3.3E + 02	0.829	n.d.	n.d.	-	-	n.d.
Fallout	YM pumice	IC60–90 02–07	1.576	1.200	1217	76	7.7E + 02	0.376	n.d.	n.d.	-	-	n.d.
Fallout	*YM pumice*	*whole IC60-90*	*4.125*	*2.920*	*2067*	*71*	*5.0E + 02*	*1.205*	*n.d.*	*n.d.*	*-*	*-*	*n.d.*

[a] Lines of entries that are entirely in italics highlight whole data on individual samples.

[b] Mt, magnetite microlite; number of asterisks indicates the presence of magnetite from a few grains (*) up to 1–2% (***); n.d., not detected.

[c] YM pumice, yellow microvesicular pumice.

ular pumices from the base of the MTN sequence, vesicle walls are broken due the existence of cracks and fractures in the groundmass. In scoriae, vesicles are mostly elongated and distorted; their walls sometimes appear deformed by the presence of microlites. The high groundmass crystallinity of some UM scoria clasts strongly affects the morphology of vesicles which, as a result, show cuspidate edges (Figure 2).

[21] Yellow and brown bands of banded pumices show textures resembling those observed in yellow microvesicular pumices and scoriae, respectively. Moderately to highly elongated vesicles characterize yellow tube pumices. Rounded vesicles are subordinated and have been frequently observed in the glassy groundmass around individual phenocrysts or mineral clots. Feldspar microlites are commonly oriented, forming alignments over the μm-to-cm-scale. Locally the feldspar alignment and vesicle orientation axis coincide.

4.2. Quantification of 2-D Textures

[22] New 2-D groundmass textural parameters (Table 1) were obtained to integrate the available data set [*Polacci et al.*, 2003; *Polacci*, 2005; *D'Oriano et al.*, 2005; *Piochi et al.*, 2005b]. The new data well compare with results previously obtained on the same rocks. However, they provide further information on (1) crystallinity of the AMS and CI groundmasses; (2) the texture of vesicles and microlites in AMS yellow tube and MTN banded pumices; and (3) vesicle and microlite textural data of the same pumices and scoriae analyzed for major, trace and volatile composition of their glassy groundmass. The overall data set highlights textural heterogeneities among different clasts, as well as within different areas of individual clasts. In general, the vesicularity increases from MTN scoriae to MTN (LMinf, Table 1), AMS and CI yellow microvesicular pumices. This increase is associated with a decrease in groundmass crystallinity (see also Figure 2).

[23] The integration of new and literature data [see also *Polacci et al.*, 2003; *Polacci*, 2005] evidences that CI pumices have vesicularities from 71% (Table 1) up to 80–90% and vesicle number densities in the order of 10^2-10^3 mm^{-2} [see also *Polacci et al.*, 2003]. The groundmass is pure glassy and microlite-free (Figure 2, and previous description in section 4.1). The AMS yellow microvesicular pumices are characterized by vesicularities in the range of 69–80% [see also *Polacci*, 2005]. Yellow tube pumices and

zones with highly elongated vesicles can also exhibit vesicularity values as low as 35–40% (Table 1). Vesicle number densities are in the range of 10^2-10^3 mm^{-2} [see also *Polacci*, 2005]. Microlites are <2%.

[24] The MTN yellow microvesicular pumices have higher vesicularity and lower groundmass crystallinity (in the range of 68–80% and 1–26%, respectively, Table 1) than the MTN scoriae (in the range 41–60% and 26–32%, respectively, Table 1). *D'Oriano et al.* [2005] also report 95% of groundmass crystallinity in blocky scoria clasts that were not analyzed in the present work. The MTN banded pumices, especially in the lowermost portion of the sequence, contain yellow and brown sectors with lower and higher microlites abundance, respectively (see Figure 2 and Table 1). The new data also show that yellow microvesicular pumices from the lowermost portion of the MTN sequence have vesicularity values of ~80% and very low microlite content (1–2%; Table 1), thus approaching values of the AMS yellow microvesicular pumice clasts. Vesicle and microlite number densities of the studied MTN pumices vary from 10^2 to 10^3 mm^{-2}; corresponding values for scoriae are mostly in the order of 10^3 mm^{-2}.

4.3. Observation and Quantification of 3-D Textures

[25] Images extracted from the 3-D digital volumes, along with the obtained 3-D textural parameters, are shown in Figure 3. Internal views of the textures of both CI and AMS yellow microvesicular pumices exhibit a highly vesicular 3-D network of small ($10^{-3}-10^{-4}$ mm^3 by volume), finely packed, coalesced (~90% vesicle connectivity) and slightly deformed to deformed vesicles. The vesicularity ranges from 73 to 76 vol% and the vesicle number density is high, about 10^4 mm^{-3} (Figure 3). Banded pumice and scoria products from the LM and UM of the MTN sequence have lower vesicularities (38–46 vol%) and number densities ($\approx10^3$ mm^{-3}) with respect to CI and AMS samples. In addition, vesicles in these clasts are larger and have irregular shapes. Despite the lower vesicularities, these samples also display a high vesicle interconnectivity, up to 95% (Figure 3). Furthermore, the AMS and CI yellow microvesicular pumices have a V_g/V_m (volume of gas/volume of matrix) ratio much higher than the MTN samples (Figure 3). Vesicularities obtained by 2-D and

3-D imaging of our samples are comparable (Table 1 and Figure 3).

4.4. Compositional Data on the Groundmass

[26] The MTN, AMS and CI groundmass has a trachy-phonolitic composition overlapping that of whole rocks (Figure 4a; new major oxides in Table 2). The SiO_2 content varies in the range of $\sim$59–62 wt% and $\sim$60–63 wt% in the AMS products and CI yellow microvesicular pumices, respectively. In the MTN products, SiO_2 varies from $\sim$58 to 64 wt%, with the UM scoriae having a slightly higher SiO_2 content. The alkali content (Na_2O+K_2O) varies from $\sim$12 to 16 wt%, although AMS clasts show higher K_2O content ($\sim$8–9 wt%) with respect to MTN products ($\sim$6–8 wt%) having a similar fractionation index (Figure 4b). K_2O in CI products shows a bimodal distribution, with values both overlapping those of MTN products and exceeding 9 wt%. Yellow and brown bands of the MTN banded pumices show a similar major element compositional range. Furthermore, glass hosting elongated and rounded vesicles in AMS yellow tube pumices has the same major element content (Table 2).

[27] The groundmass of MTN and AMS samples shows variable trace element concentration (Table 3 and Figure 5). K-rich AMS yellow pumice types are characterized by lower trace element abundances and a homogeneous composition. In contrast, MTN products evidence a wider range in trace element content, with LM clasts and UM scoriae representing the less and the more enriched terms, respectively.

[28] Both AMS and UM-MTN rocks show strongly fractionated LREE patterns with negative Eu anomaly, which is more pronounced in the MTN groundmass (Figure 5a). Instead, these products show significant differences in terms of HREE fractionation. In particular, the HREE pattern has a negative slope in microlite-poor AMS differentiates (which have $(Gd/Lu)_N$ values higher than 1), whereas it is flat or U-shaped in the microlite-rich MTN products (which have $(Gd/Lu)_N$ and $(Dy/Lu)_N$ $\sim$1 and $\leq$1, respectively).

[29] Primitive-mantle normalized patterns (Figure 5b) are strongly enriched in LREE, alkaline elements (Cs and Rb), Th and U, and show deep negative Ba and Sr anomalies. The Sr and Ba negative spikes become more pronounced moving from AMS to MTN.

4.5. Groundmass Volatiles

[30] H_2O is the most abundant volatile in all the investigated matrices; other species are Cl and F (Figure 6; average values and standard deviations reported in Table 4).
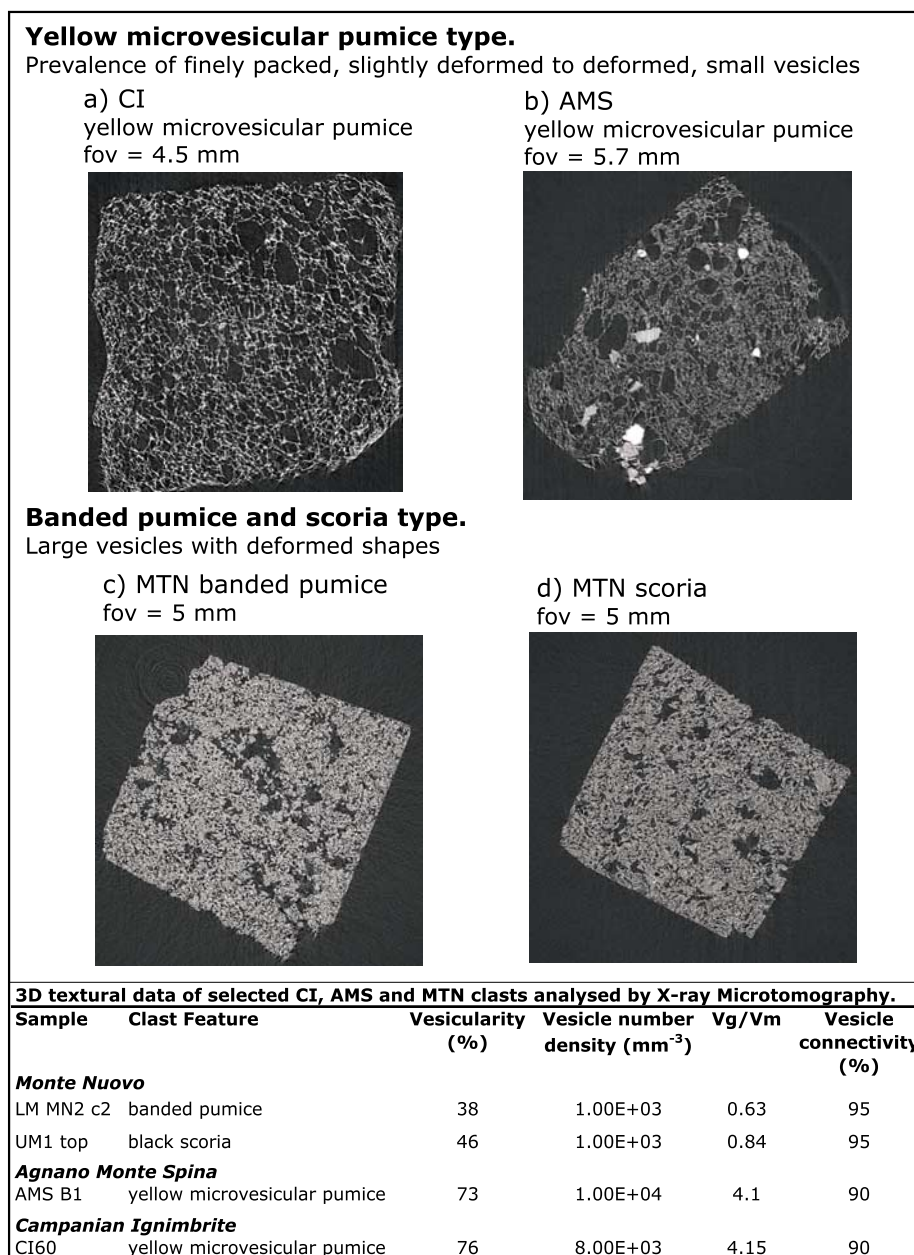
[31] The residual water content measured by SIMS varies among the different samples; values for MTN samples agree with the few literature data on MTN matrices by FT-IR [see *Piochi et al.*, 2005b]. AMS and MTN yellow microvesicular pumice clasts show the largest heterogeneity with values of 1.03 ± 0.79 and 1.41 ± 0.82 wt%, respectively (Table 4). The MTN products from the lowermost portion of the sequence are more homogeneous with residual H_2O contents of 1.11 ± 0.16 wt% (Table 4). MTN yellow bands of banded pumices show values of 1.17 ± 0.23 and 1.32 ± 0.19 wt% comparable to that of yellow microvesicular pumice (Table 4). Scoriae and brown glass in MTN banded pumices show the lowermost residual water content, 0.21 ± 0.05 wt% and below 0.59 ± 0.19 wt%, respectively (Table 4). A water content of 0.3–0.6 wt% has been reported in the literature for the CI fallout glassy matrix [*Signorelli et al.*, 2001].

[32] The MTN groundmass shows a lower Cl content (0.30 ± 0.16 to 0.69 ± 0.03 wt%) than the AMS (0.73 ± 0.19 wt%) and CI products (0.70 ± 0.11 to 0.84 ± 0.06 wt%) (Table 4).

[33] Fluorine is 0.20 ± 0.03 wt% in the AMS yellow microvesicular pumices, varies from 0.24 ± 0.13 to 0.28 ± 0.08 wt% in the CI yellow microvesicular pumices, between 0.33 ± 0.19 and 0.47 ± 0.02 wt% in the MTN pumice types, and is 0.14 ± 0.05 wt% in the MTN scoriae (Table 4).

[34] Several petrochemical features, among which (1) the sharp alternation of yellow and brown bands in banded pumices with different residual in situ water content, (2) the OH^--H_2O bond in MTN groundmasses [*Piochi et al.*, 2005b] and (3) the overall positive correlation between H_2O and Cl (Figure 6) suggest that hydration by meteoric water does not significantly affect the residual H_2O content of our rocks.

[35] On the other hand, a variable residual water content is not unusual in volcanic glassy matrices [see, e.g., *Gerlach et al.*, 1996] and also characterizes trachytic melt inclusions hosted in CI, AMS and MTN phenocrysts (from few to 3.8 wt%) [*Papale and Gresta*, 2006; Roach and Rutherford,

Yellow microvesicular pumice type.
Prevalence of finely packed, slightly deformed to deformed, small vesicles

a) CI
yellow microvesicular pumice
fov = 4.5 mm

b) AMS
yellow microvesicular pumice
fov = 5.7 mm

Banded pumice and scoria type.
Large vesicles with deformed shapes

c) MTN banded pumice
fov = 5 mm

d) MTN scoria
fov = 5 mm

3D textural data of selected CI, AMS and MTN clasts analysed by X-ray Microtomography.

| Sample	Clast Feature	Vesicularity (%)	Vesicle number density (mm^{-3})	Vg/Vm	Vesicle connectivity (%)
Monte Nuovo					
LM MN2 c2	banded pumice	38	1.00E+03	0.63	95
UM1 top	black scoria	46	1.00E+03	0.84	95
Agnano Monte Spina					
AMS B1	yellow microvesicular pumice	73	1.00E+04	4.1	90
Campanian Ignimbrite					
CI60	yellow microvesicular pumice	76	8.00E+03	4.15	90

Figure 3. (top) Tomographic images of 3-D reconstructed volumes of yellow microvesicular pumices from (a) CI and (b) AMS and of (c) LM banded pumice and (d) UM scoria from the MTN sequence. Horizontal field of view (fov) reported in each image. (bottom) Three-dimensional textural data of the analyzed rocks. Vg, volume of vesicles (gas); Vm, volume of matrix (melt).

submitted manuscript, 2007; M. Rutherford, personal communication, 2007].

[36] Furthermore, these observations converge to indicate that the detected water variation is a compositional feature acquired during the development of the volcanic processes.

[37] The bulk residual water content measured on remelted samples via FT-IR is variable (Table 4):

3 wt% in the MTN yellow microvesicular pumice, 2.3 wt% in the MTN banded pumice, 0.75 wt% in the AMS yellow microvesicular pumice and 0.6 wt% in the MTN black scoria. In principle, the applied FT-IR technique is not conventional and caution is therefore required in using the obtained data; nevertheless, we want to stress that the in situ and bulk residual values are consistent for the MTN scoria and AMS microvesicular pumice within the analytical uncertainties, especially if uncertainties
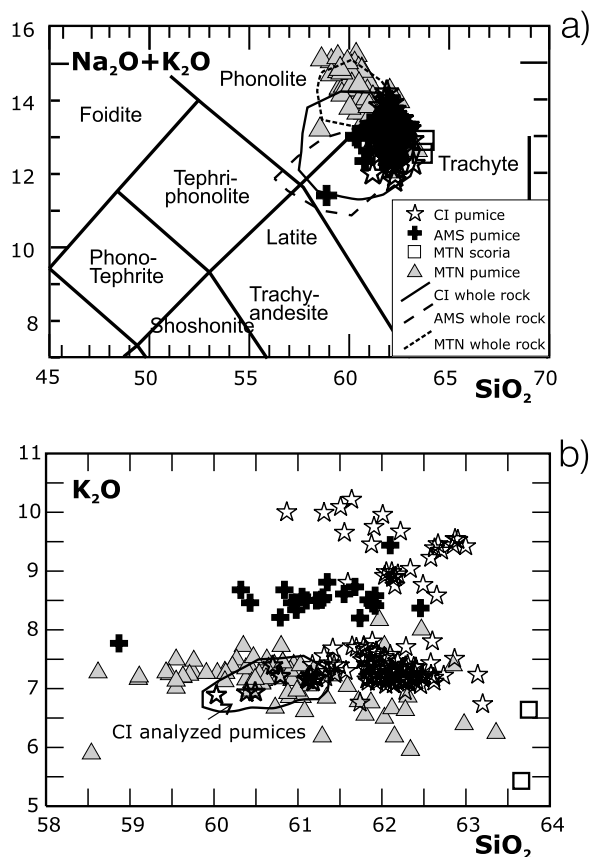
Figure 4. (a) Portion of the TAS classification diagram [*Le Bas et al.*, 1986] and (b) K_2O (wt%) versus SiO_2 (wt%) content of CI, AMS, and MTN glassy matrix. In both diagrams, the entire set of CI microprobe analyses from *Pappalardo* [1994], *Signorelli et al.* [2001], and *Polacci et al.* [2003] is shown. Fields in Figure 4a define bulk rock compositions of the investigated rocks: CI from *Civetta et al.* [1997] and *Signorelli et al.* [2001]; AMS from *de Vita et al.* [1999]; MTN from *Rosi and Sbrana* [1987] and *D'Oriano et al.* [1995]. The arrow in Figure 4b indicates the compositional field of the analyzed CI yellow microvesicular pumices from *Polacci et al.* [2003].

concerning the efficiency in removing phenocrysts from samples are considered (see section 3 and Appendix A).

[38] Discrepancies between the SIMS and FT-IR data likely derive from the need of acquiring a statistically representative number of measurements of the residual water content when H_2O is highly variable within the glassy matrix. In addition, the occurrence of hydrous and melt-inclusion-bearing microcrysts within the groundmass can also produce the observed discrepancies, increasing the residual bulk values. Therefore, it is concluded that the FT-IR data potentially provide a

reliable estimate of the groundmass residual water content. However, the detected variability suggests that future detailed investigations should be carried out to properly constrain the residual volatile content in CF products.

[39] Finally, FT-IR spectra for the analyzed groundmass samples do not show molecular CO_2 or carbonate peaks above the background, in agreement with results from CF melt inclusions with trachytic compositions showing generally <50 ppm of CO_2 [*Papale and Gresta*, 2006]. Only in AMS melt inclusions the CO_2 content ranges from few to, subordinately, hundreds of ppm [*Papale and Gresta*, 2006; M. Rutherford, personal communication, 2007].

4.6. Compositional Data on Feldspar Microlites

[40] The mineral chemistry of the studied rocks is well known [*de Vita et al. 1999*; *D'Oriano et al.*, 2005; *Piochi et al.*, 2005b]. Here we will present new data (Table 5) only to supplement the literature data set. These new data are related to (1) AMS microlites for which major element mineral chemistry is still lacking and (2) microlites in the less crystallized glassy matrices of LM pumices and scoria clasts from MTN.

[41] The analyzed MTN and AMS feldspar microlites overlap the chemical range reported in the literature (Figure 7). The whole data set can be summarized as follows: Ab_{53-56} plagioclase and Or_{40-53} alkali-feldspar are the most abundant microlite phases (up to 90%). In some cases, feldspar microlites have a composition similar to that of phenocrysts (Or_{46}) [*D'Oriano et al.*, 2005; *Piochi et al.*, 2005b]. On the basis of the Solvcalc algorithm [*Shaoxiong and Nekvasil*, 1994] and the solution model of *Elkins and Grove* [1990], the estimated equilibrium temperatures for MTN microlites are between 900 and 1000°C. These temperatures are higher than those based on feldspar phenocrysts, which point to T = 850 ± 40 °C and P_{H_2O} = 100–200 MPa [*Piochi et al.*, 2005b; *D'Oriano et al.*, 2005]. These thermobarometric estimates on feldspar phenocrysts coincide with those for crystallization within the CI magma chamber [*Civetta et al.*, 1997]. The composition of AMS microlites results from equilibrium temperatures of ∼900 ± 40°C, which are similar to those calculated from feldspar phenocrysts (896–911 ± 40°C).

Table 2. Major Elements in the Glassy Matrix of MTN and AMS Products by Electron Microprobe[a]

| Eruption Sample	Monte Nuovo LMintfb		Monte Nuovo LMintfb		Monte Nuovo LM MN2 c1		Monte Nuovo LM c2		Monte Nuovo LM c2		Monte Nuovo UM1 MN4 top		Agnano Monte Spina FL 1c		Agnano Monte Spina Fl1a	
Clast type	brown band		yellow band		yellow microvesicular pumice		yellow band		brown band		black scoria		yellow tube pumice		yellow tube pumice	
Spot n.	8		8		15		13		24		2		10		10	
	average	st dev	average	st dev	average	st dev	average	st dev	average	st dev	average	st dev	average	st dev	average	st dev
SiO_2	60.91	0.92	60.91	0.49	60.61	0.79	60.82	1.15	60.83	1.22	63.71	0.06	61.10	0.50	61.52	0.45
TiO_2	0.39	0.09	0.42	0.05	0.42	0.07	0.45	0.08	0.43	0.08	0.31	0.04	0.42	0.04	0.48	0.03
Al_2O_3	19.32	0.52	19.13	0.23	19.70	0.29	19.18	0.64	19.29	0.53	19.91	0.46	18.40	0.17	18.15	0.55
FeO	2.89	0.79	2.80	0.25	3.04	0.57	3.11	0.80	3.06	0.75	1.63	0.25	3.46	0.27	3.53	0.17
MnO	0.24	0.07	0.24	0.06	0.25	0.06	0.28	0.09	0.27	0.10	0.07	0.04	0.13	0.05	0.18	0.03
MgO	0.22	0.07	0.22	0.03	0.23	0.05	0.24	0.08	0.25	0.08	0.12	0.00	0.62	0.11	0.64	0.06
CaO	1.90	0.49	1.98	0.26	1.81	0.29	1.93	0.32	2.00	0.29	1.55	0.10	2.61	0.24	2.60	0.13
Na_2O	7.05	0.45	7.06	0.25	6.68	0.43	7.00	0.63	6.81	0.62	6.67	0.61	4.48	0.36	4.35	0.17
K_2O	7.09	0.58	7.22	0.32	7.24	0.38	6.95	0.35	7.05	0.48	6.04	0.86	8.67	0.29	8.45	0.17
P_2O_5	0.04	0.02	0.04	0.03	0.02	0.01	0.03	0.02	0.04	0.02	0.01	0.00	0.11	0.05	0.11	0.04
Total	99.42	1.00	99.37	0.94	96.89	1.14	97.32	0.85	97.89	1.04	98.75	0.37	97.66	2.30	97.23	1.01

[a] Spot n., number of spot analyses in each investigated clast; st dev, standard deviation. Low number of spots in UM1MN4 top is due to the high crystallization of the groundmass.

Table 3. Trace and REE Elements in the Glassy Matrix of AMS and MTN Products by LA ICP-MS[a]

Eruption Sample / Clast type / Spot n.	Agnano Monte Spina AMS B1 yellow microvesicular pumice 7		Monte Nuovo LMinf b yellow band 19		Monte Nuovo LMinf yellow microvesicular pumice 8		Monte Nuovo LMinf yellow microvesicular pumice 4		Monte Nuovo LM MN2 c1 yellow microvesicular pumice 15		Monte Nuovo LMMN2 c2 brown band 8		Monte Nuovo LMMN2 c2 yellow band 10		Monte Nuovo UMMN4top black scoria 6		Monte Nuovo UMMN4 black scoria 9	
	average	st dev	average	st dev	average	st dev	average	st dev	average	st dev	average	st dev	average	st dev	average	st dev	average	st dev
Li	58.38	12.05	115.31	26.65	114.72	23.60	104.68	15.37	101.58	9.31	113.92	13.39	105.15	13.79	125.11	12.03	159.64	33.05
B	89.60	14.30	724.83	935.04	223.03	32.91	214.29	52.28	166.44	12.08	181.42	19.88	180.16	44.27	261.38	33.93	215.81	58.09
Sc	4.56	1.42	2.22	0.69	2.60	1.45	1.82	0.64	2.20	0.39	2.02	0.96	2.39	0.74	1.70	0.57	2.89	2.31
V	52.36	10.93	20.73	5.22	20.23	1.23	18.47	1.93	17.35	1.47	18.89	1.18	17.51	2.31	19.41	2.39	32.64	15.85
Cr	6.06	1.02	15.10	13.31	16.57	1.63	-	-	3.36	1.28	4.24	4.07	2.70	2.56	16.37	0.00	6.36	3.17
Co	6.54	7.39	1.97	1.83	1.25	0.82	0.83	0.33	0.89	0.27	1.66	1.46	1.59	1.84	1.26	0.48	1.72	0.92
Ni	7.48	8.27	2.80	4.47	2.64	1.81	9.46	0.00	2.32	4.21	0.71	0.32	3.64	6.64	1.87	0.74	2.74	1.17
Zn	82.80	87.71	108.10	25.68	115.08	31.85	86.41	26.31	126.52	38.42	132.11	24.33	117.86	7.89	146.75	32.67	165.61	57.99
Rb	399.27	39.58	615.12	140.47	613.71	47.84	613.49	36.80	541.60	32.72	562.21	41.98	528.32	75.92	651.53	56.91	711.37	155.59
Sr	247.23	36.20	4.32	2.10	6.68	3.25	7.43	5.04	2.22	0.55	1.85	0.53	2.90	1.40	4.37	2.36	6.36	3.37
Y	33.10	4.90	55.74	12.45	58.70	7.97	61.34	6.47	45.10	4.33	53.01	0.78	48.87	10.04	64.34	5.98	78.11	26.72
Zr	488.14	62.25	924.66	188.50	993.49	164.26	964.22	106.44	774.88	63.26	886.40	15.43	819.72	134.60	1097.60	115.47	1370.92	329.05
Nb	65.49	7.79	150.05	29.45	150.86	14.33	148.56	7.30	136.57	9.36	155.28	4.33	138.49	16.66	175.64	22.18	222.27	65.91
Cs	31.00	3.61	71.24	19.75	67.54	6.48	62.01	6.40	57.67	4.19	61.86	7.82	54.03	12.69	48.31	6.00	42.98	3.09
Ba	203.32	37.78	1.92	1.14	4.83	3.43	0.75	0.19	0.38	0.37	0.75	0.48	0.83	0.29	0.44	0.11	4.92	5.29
La	92.97	11.26	175.74	35.65	182.51	17.61	186.51	8.22	157.24	11.61	172.70	4.69	158.69	23.98	197.03	17.04	259.19	63.62
Ce	175.48	18.74	332.13	65.64	332.08	23.16	328.46	8.76	306.83	19.51	342.75	17.61	312.11	36.66	370.54	36.76	492.20	118.72
Pr	16.20	1.93	29.93	6.03	30.79	3.04	31.55	1.11	27.32	1.82	30.99	1.28	28.38	4.33	33.63	2.81	47.61	10.16
Nd	58.35	5.27	95.67	18.72	99.83	8.31	98.59	3.72	86.12	7.87	98.72	4.06	89.29	12.17	105.46	9.70	163.27	48.98
Sm	10.08	2.00	15.65	4.09	15.58	2.39	14.88	1.56	13.51	1.90	15.37	0.78	13.86	2.53	17.10	2.41	27.12	8.13
Eu	1.47	0.19	1.09	0.28	1.23	0.33	1.84	0.75	1.17	0.17	1.01	0.25	0.99	0.23	1.32	0.42	1.09	0.46
Gd	6.43	1.27	10.02	2.35	11.65	1.29	12.92	2.44	8.92	1.46	10.40	0.88	9.81	2.36	13.21	1.41	17.10	5.95
Tb	0.86	0.21	1.58	0.33	1.58	0.36	1.47	0.52	1.37	0.16	1.64	0.24	1.56	0.25	1.84	0.40	2.77	0.46
Dy	6.28	1.24	9.34	1.96	9.47	1.40	10.37	2.29	8.03	1.34	9.29	1.34	8.78	1.63	11.03	1.06	13.17	3.53
Ho	1.11	0.15	1.94	0.44	2.07	0.30	2.22	0.62	1.66	0.33	1.90	0.20	1.78	0.32	2.38	0.35	3.42	1.54
Er	3.49	0.82	5.65	1.55	5.34	1.20	5.68	1.12	4.89	1.04	5.28	0.42	5.13	0.85	6.22	1.33	10.33	3.04
Tm	0.46	0.16	0.87	0.24	0.82	0.21	0.92	0.21	0.74	0.16	0.86	0.15	0.83	0.16	0.95	0.24	1.44	0.52
Yb	2.73	0.66	6.23	1.40	6.68	1.76	5.91	2.74	5.68	0.64	6.59	0.73	5.63	1.30	7.39	1.51	10.73	2.85
Lu	0.42	0.17	0.97	0.27	1.03	0.22	0.77	0.23	0.86	0.11	0.96	0.08	0.87	0.22	1.10	0.15	1.78	0.62
Hf	8.65	2.10	18.39	4.27	20.57	4.53	20.51	3.45	15.34	2.02	17.96	0.71	17.29	2.82	20.89	1.17	33.12	9.06
Ta	3.04	0.73	5.50	1.10	5.65	0.43	5.49	0.72	4.90	0.62	5.60	0.37	5.44	0.70	6.70	0.56	9.93	3.17
Pb	58.19	5.23	105.32	22.39	103.71	8.35	89.45	14.36	83.44	6.43	88.48	3.71	88.24	7.27	131.68	23.76	168.09	24.95
Th	47.57	5.21	97.02	19.36	101.02	13.39	101.64	15.47	83.11	6.52	96.12	3.98	90.75	13.99	106.59	11.20	184.61	77.20
U	17.41	1.96	37.01	7.22	37.06	2.64	35.83	3.25	32.68	2.77	37.83	3.03	35.32	3.54	44.35	3.41	60.49	13.93

[a] Data in ppm. Spot n., number of spot analyses in each investigated sample.

Rock/Chondrites a)

Rock/Primitive Mantle b)
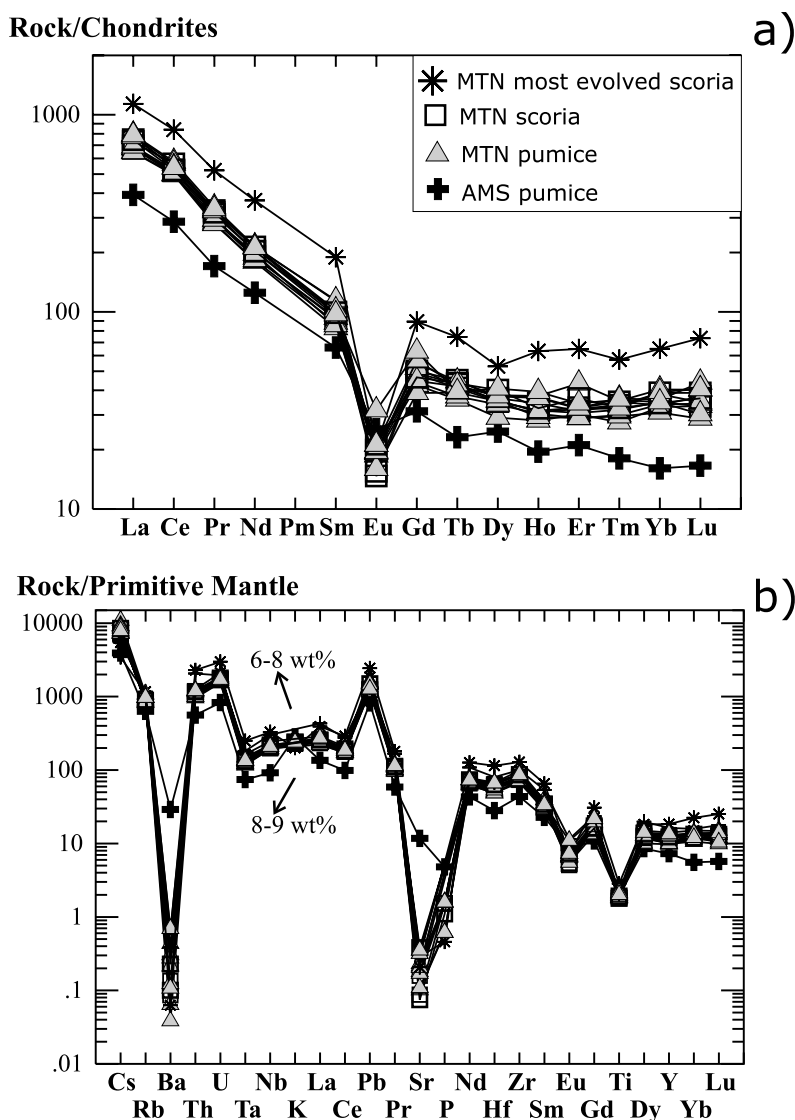
Figure 5. (a) REE concentration in AMS and MTN glassy matrix normalized to primitive mantle values [*Sun and McDonough*, 1989] and (b) normalized multielement diagrams [*Sun and McDonough*, 1989] for the same glasses. Percentages in Figure 5b are the absolute K_2O values measured in the MTN and AMS glassy matrices (Table 2). Plotted trace elements and REE data are average values as reported in Table 3 together with the related standard deviation.

4.7. Bulk-Rock and Groundmass-Derived Viscosity Data

[42] Melt composition, temperature, crystal and vesicle content, dissolved volatiles, and pressure are all parameters that influence magma viscosity to various extent. Recently, *Giordano et al.* [2008] have calibrated an empirical model capable of predicting the viscosity of a melt from its composition and volatile content (e.g., H_2O). This model is particularly suited to calculate the viscosity of CF products here investigated,

because it was calibrated on about 1850 viscosity measurements of dry and volatile-rich melts, among which those synthesized from CF volcanic products are well represented [e.g., *Romano et al.*, 2003; *Giordano et al.*, 2004].

[43] The *Giordano et al.* [2008] model, combined with models accounting for the effects of the crystal fraction and the strain rate on viscosity [*Costa et al.*, 2007; *Caricchi et al.*, 2007], has allowed us to estimate the viscosity of the CI, AMS and MTN magmas using the compositions
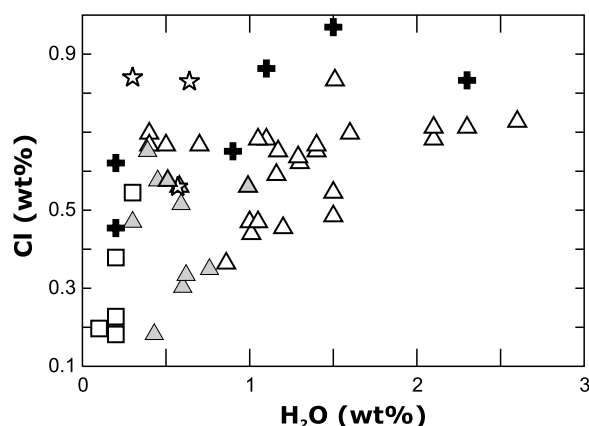
Figure 6. Cl (wt%) versus in situ H_2O content (wt%) in the glassy matrix of the investigated CI, AMS, and MTN clast types. CI data from *Signorelli et al.* [2001]. Symbols as in Figure 4. In addition, open triangles indicate yellow microvesicular pumices and/or yellow bands, and full triangles indicate brown bands of the banded pumices.

and crystallinity derived from the investigated samples. The eruptive temperatures used to calculate magma viscosity of AMS and MTN magmas come from geo-thermometric phase equilibria studies (M. Rutherford, personal communication, 2007) and are estimated to be 945 ± 39 and 890 ± 10°C, respectively. A temperature of 900 ± 30°C is reported for CI magmas by *Giordano et al.* [2004, and references therein]. Following *Papale and Polacci* [1999], melt viscosity is assumed to be independent of the dissolved carbon dioxide content as justified by the absence or low amounts of CO_2 in the studied products [*Papale and Gresta*, 2006; our data]. Figure 8 shows the effect of water content on the viscosity assuming as the residual liquid magma composition either the bulk rock (data from *de Vita et al.* [1999], *Polacci et al.* [2003], and *D'Oriano et al.* [2005]) (Figure 8a) or the glassy matrix (Table 2 and Figure 8b). The effect of the crystal content (see Table 1) on the viscosity computed from the glassy matrix is described in Figure 8c. The results highlight that, for the same water content, the viscosity of a liquid composition equivalent to that of the bulk rock (Figure 8a) is nearly identical for all magmas, with slightly lower values corresponding to AMS rocks. A similar viscosity is also calculated when assuming the glassy matrix of pumices as the liquid composition (Figure 8b). Finally, considering again the same water content, the viscosity increases at least up to 1 log unit Pa s from pumice

to scoria clasts (Figure 8b), owing to the different phenocryst and microlite content (Figure 8c).

5. Discussion

5.1. Magma Dynamics as Deduced by Vesicle Texture and Content

[44] In pyroclastic products of explosive eruptions, vesicles mainly represent gas bubbles within magma frozen in upon fragmentation [e.g., *Sparks*, 1978]. Their size, shape and distribution provide information on volatile exsolution, expansion and separation that, in the absence of differences in water solubility (as reported for CF trachytes [*Di Matteo et al.*, 2004]), depend on magma viscosity and ascent processes (e.g., degassing style, permeability development).

[45] Vesicles are randomly distributed within the investigated samples, as it is generally observed during homogeneous vesicle nucleation [*Mangan and Sisson*, 2000]. The vesicularity of the CI, AMS and basal LM-MTN yellow microvesicular pumices (Table 1 and Figure 3) approaches the critical value of 70–80% that is typical of purely magmatic fragmentation due to vesicles growth under closed-system conditions [*Sparks*, 1978; *Proussevitch et al.*, 1993]. The spherical shape of vesicles in CI and AMS (Figures 2 and 3), as well as the high V_g/V_m ratio (Figure 3), can be attributed to the internal gas overpressure generated consequently to the vesicle growth process.

[46] On the other hand, the lower vesicularity (35–64%, Table 1; ∼40%, Figure 3) and the variable vesicle shapes (Figure 3) documented in the in MTN banded pumice and scoria clasts point to a different scenario. In MTN banded pumices, the coexistence of small, spherical and large, irregular, deformed vesicles (Figures 2 and 3), suggests contemporaneous vesicle nucleation and coalescence related to gas exsolution and possibly separation. Similarly, scoria samples show a complex network of connected microcrack-like vesicles with variable sizes (Figures 2 and 3) that are thought to be responsible for the high vesicle connectivity values found in these products (see below) and that are possibly associated with gas separation.

[47] Although the vesicle connectivity of all investigated samples is high (>90%; Figure 3) and correlated with high vesicularity values for both CI and AMS pumice clasts, it must be highlighted that in the MTN products the very high connectiv-

Table 4. In Situ Residual Volatiles by SIMS and Bulk Residual Water Content by FT-IR in the CI, AMS, and MTN Products[a]

Unit	Sample Name	Spot N.	H_2O wt%		F wt%		Cl wt%		Bulk H_2O wt%
			Average	St Dev	Average	St Dev	Average	St Dev	
Monte Nuovo									
LM basal yellow microvesicular pumice	LM inf	5	1.11	0.16	0.37	0.08	0.58	0.13	3.00
LM basal brown pumice	LMinb	9	0.59	0.19	0.33	0.19	0.48	0.16	-
LM basal yellow bands	LMinb	4	1.17	0.23	0.33	0.07	0.60	0.18	-
LM yellow microvesicular pumice	LM c1	11	1.41	0.82	0.47	0.02	0.69	0.03	-
LM brown bands	LM c2	2	0.44	0.22	0.35	0.15	0.39	0.12	-
LM yellow bands	LM c2	5	1.32	0.19	0.43	0.07	0.51	0.07	-
LM banded pumice	LM c2	-	-	-	-	-	-	-	2.30
UM scoria	UM1top	5	0.21	0.05	0.14	0.05	0.30	0.16	0.60
Agnano Monte Spina									
AMS yellow microvesicular pumice	AMS B1	6	1.03	0.79	0.20	0.03	0.73	0.19	0.75
Campanian Ignimbrite									
LFU yellow microvesicular pumice[b]	-	68	0.61	0.23	0.24	0.13	0.70	0.11	-
UFU yellow microvesicular pumice[b]	-	18	0.30	0.02	0.28	0.08	0.84	0.06	-

[a] Spot n., number of spot analyses in each investigated sample; st dev, standard deviation.
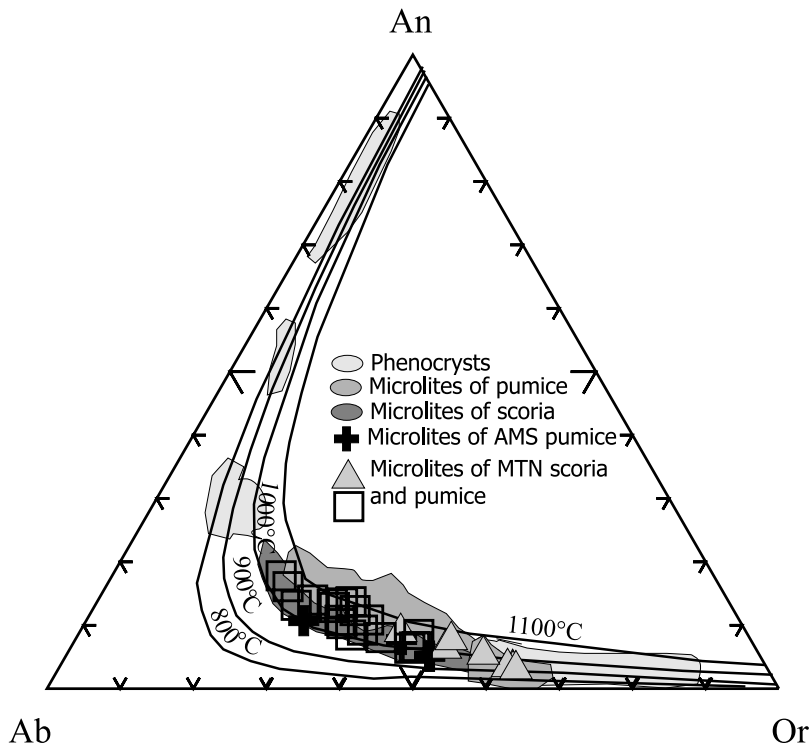[b] Data from *Signorelli et al.* [2001].

Table 5. Mineral Chemistry of MTN and AMS Products by Electron Microprobe

Unit Sample	LMinfb		LM MN2 c2							MTN6-1[a]					
Spot Type	feld5.2m micro	feld5.3m micro	feld 1c micro	feld 1r micro	feld 1r2 micro	feld 1c1 micro	feld 1r3 micro	feld2r micro	feld2c micro	mic1 micro	mic4 micro	mic5 micro	mic6 micro	mic7 micro	mic8 micro
SiO_2	63.59	65.10	65.89	65.42	66.05	65.87	65.92	63.65	65.02	64.27	63.52	64.09	63.18	63.03	62.03
TiO_2	0.20	0.15	0.07	0.06	0.07	0.04	0.04	0.18	0.10	-	-	-	-	-	-
Al_2O_3	19.44	19.23	19.19	19.28	19.15	19.39	19.06	20.03	19.56	20.77	21.59	20.83	21.42	21.71	22.78
MgO	0.06	0.00	0.02	0.00	0.00	0.01	0.00	0.02	0.00	-	-	-	-	-	-
CaO	1.86	1.29	0.67	0.62	0.65	0.69	0.62	1.66	1.12	1.33	2.19	1.30	2.12	2.58	3.66
MnO	0.05	0.03	0.00	0.00	0.02	0.00	0.00	0.02	0.02	-	-	-	-	-	-
FeO	1.00	0.34	0.18	0.19	0.17	0.14	0.23	0.52	0.24	-	-	-	-	-	-
Na_2O	5.43	4.79	3.92	3.90	4.12	3.98	3.81	4.90	4.33	5.15	6.10	5.27	6.20	6.02	6.69
K_2O	7.64	8.76	10.61	10.55	10.71	10.43	10.49	9.31	9.91	7.87	5.86	7.83	6.04	5.51	3.95
SrO	-	-	-	-	-	-	-	-	-	0.00	0.00	0.00	0.00	0.00	0.00
BaO	-	0.09	-	-	-	-	-	-	-	0.20	0.18	0.21	0.33	0.42	0.18
Total:	99.27	99.79	100.54	100.03	100.94	100.55	100.16	100.29	100.29	99.59	99.44	99.53	99.29	99.27	99.29
Fe_2O_3	0.90	0.31	0.17	0.17	0.15	0.13	0.20	0.47	0.21	0.46	0.63	0.53	0.81	0.81	0.80
FeO	-	-	-	-	-	-	-	-	-	-	-	-	-	-	-
	Number of Ions on the Basis of 32 Oxygens														
Si	11.62	11.81	11.89	11.87	11.89	11.88	11.93	11.57	11.77	11.60	11.42	11.57	11.39	11.35	11.13
Ti	0.03	0.02	0.01	0.01	0.01	0.00	0.01	0.02	0.01	0.00	0.00	0.00	0.00	0.00	0.00
Al	4.19	4.11	4.08	4.12	4.06	4.12	4.06	4.29	4.17	4.42	4.57	4.43	4.55	4.61	4.82
Fe3+	0.12	0.04	0.02	0.02	0.02	0.02	0.03	0.06	0.03	0.06	0.09	0.07	0.11	0.11	0.11
Mg	0.02	0.00	0.00	0.00	0.00	0.00	0.00	0.01	0.00	0.00	0.00	0.00	0.00	0.00	0.00
Ca	0.36	0.25	0.13	0.12	0.12	0.13	0.12	0.32	0.22	0.26	0.42	0.25	0.41	0.50	0.70
Na	1.93	1.68	1.37	1.37	1.44	1.39	1.34	1.73	1.52	1.80	2.13	1.85	2.17	2.10	2.33
K	1.78	2.03	2.44	2.44	2.46	2.40	2.42	2.16	2.29	1.81	1.34	1.80	1.39	1.27	0.90
Ba	0.00	0.01	0.00	0.00	0.00	0.00	0.00	0.00	0.00	0.00	0.00	0.00	0.00	0.00	0.00
Sr	0.00	0.00	0.00	0.00	0.00	0.00	0.00	0.00	0.00	0.04	0.04	0.04	0.07	0.09	0.04
Sum	20.05	19.95	19.95	19.96	20.01	19.94	19.90	20.17	20.02	19.95	19.97	19.98	20.02	19.93	20.00
Si+Al	15.81	15.92	15.97	15.99	15.95	16.00	15.99	15.86	15.95	16.02	15.99	16.01	15.94	15.96	15.95
An mol%	8.95	6.32	3.28	3.07	3.11	3.41	3.08	7.68	5.38	6.64	10.84	6.45	10.33	12.88	17.88
Ab mol%	47.29	42.51	34.81	34.87	35.71	35.45	34.48	41.00	37.79	46.55	54.63	47.31	54.65	54.38	59.14
Or mol%	43.76	51.17	61.90	62.06	61.18	61.14	62.44	51.32	56.83	46.80	34.53	46.24	35.03	32.74	22.98
	Recalculation to 4 Cations														
Si															
Al IV															
Fe3+ IV															
Sum T															
Al VI															
Ti															
Cr															
Fe3+															
Fe2+															
Mg															
Sum M1															
Fe2+															
Mn															
Mg															
Ca															
Na															
Sum M2															
Sum M1+M2															
Ca%															
Mg%															
Fe^{3+}, Fe^{2+}, Mn%															

[a]Data from P. Landi (personal communication, 2007).

Unit	Monte Nuovo													Agnano Monte Spina			
Sample	MTN6-1[a]						MTN3-47[a]							FL 1c			FL1a
Spot Type	mic2bis micro	mic3bis micro	mic4bis micro	mic8bis micro	mic9bis micro	mic10bis micro	mic1 micro	mic3 micro	mic4 micro	mic5 micro	mic6 micro	mic8 micro	mic2bis micro	micro2.2 micro	micro2.1 micro	micro micro	Cpx1 micro
SiO_2	64.09	63.47	63.33	63.42	63.27	64.53	63.55	63.79	64.15	63.14	62.82	64.21	64.68	64.46	64.99	66.00	50.85
TiO_2	-	-	-	-	-	-	-	-	-	-	-	-	-	0.09	0.10	0.08	0.73
Al_2O_3	20.82	21.66	21.48	21.60	21.70	21.11	21.54	21.68	21.12	21.94	22.43	20.86	20.73	20.46	19.93	19.39	3.49
MgO	-	-	-	-	-	-	-	-	-	-	-	-	-	0.01	0.02	0.01	12.85
CaO	1.74	2.81	2.58	2.71	2.71	2.15	2.48	2.62	1.87	2.77	3.25	1.62	1.72	2.31	1.64	1.13	22.81
MnO	-	-	-	-	-	-	-	-	-	-	-	-	-	0.00	0.00	0.00	0.49
FeO	-	-	-	-	-	-	-	-	-	-	-	-	-	0.46	0.42	0.50	8.61
Na_2O	5.02	6.28	6.44	6.07	6.73	5.52	5.73	5.64	5.82	5.74	6.57	5.55	6.05	6.95	5.41	5.26	0.47
K_2O	7.87	4.91	5.36	5.46	4.71	6.36	6.02	5.43	6.49	5.84	4.19	6.95	6.29	5.24	7.67	8.77	-
SrO	0.00	0.00	0.00	0.00	0.00	0.00	0.00	0.00	0.00	0.00	0.00	0.00	0.00	-	-	-	-
BaO	0.08	0.16	0.17	0.14	0.17	0.00	0.21	0.23	0.12	0.15	0.12	0.11	0.00	-	-	-	0.03
Total:	99.62	99.29	99.36	99.40	99.29	99.67	99.53	99.39	99.57	99.58	99.38	99.30	99.47	99.98	100.16	101.14	100.33
Fe_2O_3	0.37	0.70	0.64	0.60	0.71	0.33	0.47	0.61	0.43	0.43	0.63	0.69	0.53	0.41	0.37	0.45	1.63
FeO	-	-	-	-	-	-	-	-	-	-	-	-	-	-	-	-	7.11
Number of Ions on the Basis of 32 Oxygens																	
Si	11.57	11.39	11.39	11.40	11.36	11.57	11.44	11.45	11.54	11.37	11.27	11.58	11.62	11.57	11.70	11.81	
Ti	0.00	0.00	0.00	0.00	0.00	0.00	-	-	-	-	-	-	-	0.01	0.01	0.01	
Al	4.43	4.58	4.55	4.58	4.59	4.46	4.57	4.59	4.48	4.66	4.74	4.43	4.39	4.33	4.23	4.09	
Fe3+	0.05	0.09	0.09	0.08	0.10	0.04	0.07	0.09	0.06	0.06	0.09	0.10	0.08	0.06	0.05	0.06	
Mg	0.00	0.00	0.00	0.00	0.00	0.00	-	-	-	-	-	-	-	0.00	0.00	0.00	
Ca	0.34	0.54	0.50	0.52	0.52	0.41	0.48	0.50	0.36	0.53	0.62	0.31	0.33	0.45	0.32	0.22	
Na	1.76	2.18	2.25	2.12	2.34	1.92	2.00	1.96	2.03	2.00	2.29	1.94	2.11	2.42	1.89	1.82	
K	1.81	1.12	1.23	1.25	1.08	1.45	1.38	1.24	1.49	1.34	0.96	1.60	1.44	1.20	1.76	2.00	
Ba	0.00	0.00	0.00	0.00	0.00	0.00	0.00	0.00	0.00	0.00	0.00	0.00	0.00	0.00	0.00	0.00	
Sr	0.02	0.03	0.04	0.03	0.04	0.00	0.01	0.02	0.01	0.01	0.01	0.01	0.00	0.00	0.00	0.00	
Sum	19.96	19.91	20.01	19.94	19.99	19.86	19.96	19.86	19.98	19.98	19.98	19.98	19.96	20.03	19.97	20.02	
Si+Al	16.00	15.97	15.95	15.97	15.95	16.03	16.02	16.04	16.02	16.02	16.01	16.01	16.00	15.90	15.93	15.90	
An mol%	8.62	14.04	12.51	13.42	13.22	10.91	12.39	13.58	9.29	13.77	16.15	8.13	8.53	10.95	7.99	5.35	
Ab mol%	44.98	56.77	56.53	54.39	59.42	50.68	51.80	52.91	52.32	51.65	59.07	50.37	54.31	59.50	47.61	45.11	
Or mol%	46.40	29.20	30.96	32.19	27.36	38.42	35.81	33.51	38.39	34.58	24.79	41.50	37.15	29.55	44.41	49.54	

Recalculation to 4 Cations

Si		1.90
Al IV		0.10
Fe3+ IV		0.00
Sum T		2.00
Al VI		0.05
Ti		0.02
Cr		0.00
Fe3+		0.05
Fe2+		0.17
Mg		0.71
Sum M1		1.00
Fe2+		0.05
Mn		0.00
Mg		0.00
Ca		0.91
Na		0.03
Sum M2		1.00
Sum M1+M2		2.00
Ca%		48.12
Mg%		37.72
Fe^{3+}, Fe^{2+}, Mn%		14.17

Figure 7. Ternary diagram for feldspar phenocrysts and microlites from CI, AMS, and MTN rocks. Lines are solvi calculated by the Solvcalc algorithm [*Shaoxiong and Nekvasil*, 1994]. Grey areas exhibit literature data: in light grey, data from *Civetta et al.* [1997] (CI phenocrysts), *de Vita et al.* [1999] (AMS phenocrysts), *D'Oriano et al.* [2005], and *Piochi et al.* [2005b] (MTN phenocrysts); in intermediate and dark grey, data from *D'Oriano et al.* [2005] and *Piochi et al.* [2005b] (microlites in MTN pumice and scoria, respectively). Note that the Ab-richer feldspars from holocrystalline dense scoria described by *D'Oriano et al.* [2005] have not been reported. Symbols as in Figure 4. New AMS and MTN data for microlites from Table 5.

ity (>95%) is associated with a lower vesicularity. This observation is consistent with results from degassing experiments [*Burgisser and Gardner*, 2005, and references therein] in which the process of vesicle coalescence is shown to be dependent on both time and porosity. In particular, these experiments demonstrated that under open-system degassing vesicle coalescence can develop at a relatively low vesicularity (~40%). Efficient volatile escape from the magmatic system is considered a crucial process to lowering the eruption explosivity [*Eichelberger et al.*, 1986]. Therefore, our observation suggests that vesiculation in trachytic melts from low to moderately explosive eruptions at CF occurred under open-system conditions and was essentially controlled by gas exsolution (partitioning of volatiles dissolved in the melt in a distinct gas phase) along the conduit and outgassing (separation of the gas phase from the magma body) through the conduit and at the vent. The occurrence of the complex network of interconnecting vesicles reported above, along with the higher groundmass crystallinity (Table 1) and the

low residual water content (Table 4) of the MTN clasts further supports this idea.

[48] Finally, the existence of yellow tube pumices in the CI, AMS and MTN LM deposits suggests that the magma also experienced high strain rates in response to rapid decompression and, in turn, rapid ascent rate from the storage level through the conduit [*Alidibirov and Dingwell*, 1996, 2000; *Spieler et al.*, 2004]. Yellow tube pumices are more likely to develop at the conduit walls where the higher shear stress imparts a greater deformation to the magma [*Cashman et al.*, 2000; *Polacci et al.*, 2003]. Ultimately, it is here suggested that stretching of the magma may promote the formation of the heterogeneous vesicle textures that we observe within each single tube pumice clast (Table 1).

5.2. Magma Dynamics as Deduced by Microlite Texture and Content

[49] Degassing-induced undercooling has been invoked for the MTN magmas on the basis of their mineral chemistry [*Piochi et al.*, 2005b; *D'Oriano*
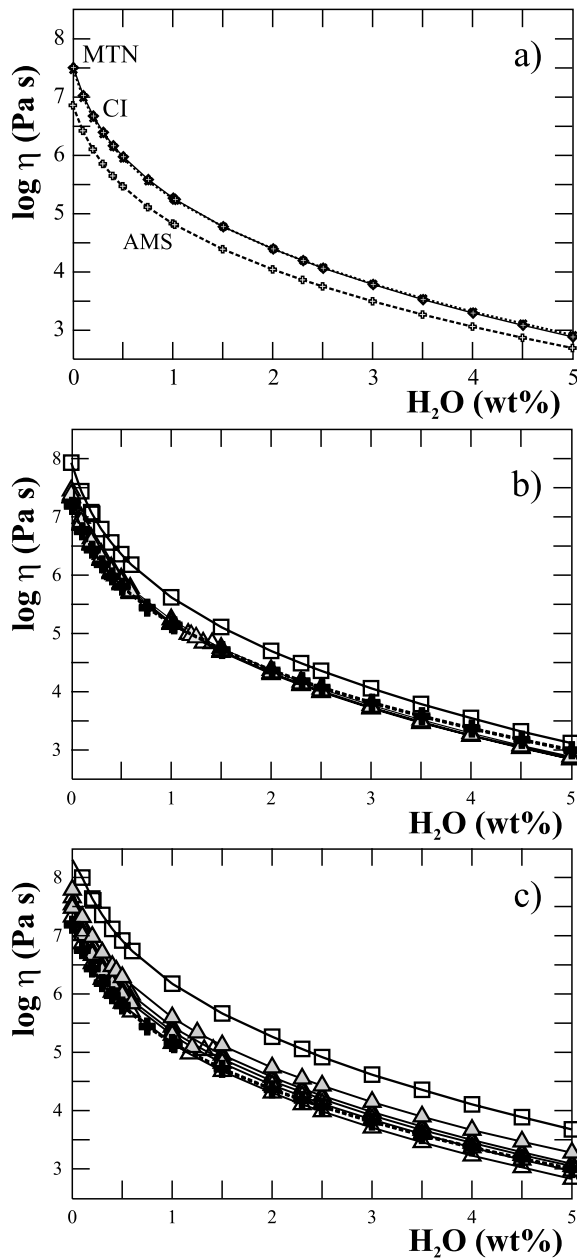
Figure 8. Calculated viscosities (Pa s) versus H_2O (wt%) at eruptive temperatures for the investigated CI, AMS, and MTN rocks (see text for further details). (a) Liquid viscosity of the equivalent bulk-rock. (b) Viscosity of the residual microlite-free matrix. (c) Viscosity of the matrix + phenocrysts + microlites mixture. Symbols in Figures 8b and 8c as in Figure 6.

lites (Figure 7). This shift toward higher Ca content of feldspar microlites cannot be related to heating, because there is no evidence that significantly hotter magma recharged the storage reservoirs [*Civetta et al.*, 1997; *de Vita et al.*, 1999; *Piochi et al.*, 2005b; *D'Oriano et al.*, 2005], nor to cooling that would result in the opposite trend. Therefore, undercooling can be a result of the crystallization driven by magma decompression. The occurrence of decompression-induced undercooling is further supported by a) the total or nearly total absence of hydrous minerals in microlite assemblages and b) the lower H_2O content in the products with higher groundmass crystallinity (Table 4; see also section 5.4).

[50] The *Housh and Luhr* [1991] algorithm gives coherent solutions for plagioclase phenocrysts-glass pairs, suggesting a water content of 3.9–3.6 wt% at 850–900°C. Unfortunately, the algorithm does not provide realistic estimates when applied to alkali-feldspar microlites and glass, perhaps because it is based on plagioclase crystallization in equilibrium with the melt. Anyway, if we take into account only the Ab molecule, the estimated temperature of microlite crystallization requires water content <1 wt%, in agreement with the analytical data here presented on microlite-rich products (Table 4; see also section 5.4).

[51] Moreover, experiments on the kinetics of crystallization indicate that the crystal number, size and shape vary with undercooling [see *Couch et al.*, 2003]. With reference to our work, the increase of groundmass crystallinity throughout the MTN stratigraphic sequence (Figure 2 and Table 1) suggests that the rate of undercooling decreased during the progression of the eruption. In addition, the occurrence of crystal-poor pumice types is likely related to batches of magma that did not experience significant decompression-induced crystallization. It can be argued that the ascent of these magma batches to the fragmentation level was presumably so rapid that crystallization was limited or impeded [*Cashman and Blundy*, 2000; *Couch et al.*, 2003; *Geschwind and Rutherford*, 1995]. In particular, we believe that the CI magma has risen so fast to have no time to form microlites.

5.3. Geochemistry of the Glassy Matrix and Syneruptive Magma Evolution

[52] Major element glass compositions argue in favor of a genetic link between MTN and the most evolved CI glasses, in agreement with the hypothesis of *D'Antonio et al.* [1999]. However, differ-

et al., 2005]. A similar process can be suggested for the AMS magmas. In fact, both cases are characterized by the relocation of the position of the microlite feldspar solvus curves toward higher or slightly higher temperatures in comparison to those of phenocryst feldspars (see section 4.6), as highlighted by the higher Ca contents of the micro-

ences in the K_2O/Na_2O ratio (1–3, ~2 and ~1 for CI, AMS and MTN, respectively) indicate that AMS and MTN magmas represent distinct batches of magma, as also suggested by *Pappalardo et al.* [2002] on the basis of Sr-isotope data. The differences in chemical composition between AMS and MTN parental melts may be related either to their origin from distinct mantle sources or to a slightly different evolution history within the magmatic system [*Pappalardo et al.*, 2002].

[53] Trace element data (Table 3 and Figures 5a and 5b) highlight that the most differentiated microlite-richer MTN scoriae display a significant enrichment of incompatible elements and a flat or U-shaped fractionation of HREE patterns with respect to the least evolved microlite-poorer products. Moreover, all MTN products are highly depleted in Ba and Sr in comparison to the less evolved trace element compositions recorded by AMS glasses. These data support the hypothesis that the analyzed CF glasses represent melts that evolved via fractional crystallization of the observed feldspar microlites from parental magmas with only slightly different trace element signatures. Reliable data of partition coefficients ($^{mineral/liquid}D$) between feldspars and a trachy-phonolitic melt from both natural and experimental systems are still scarce. Available values of partition coefficients ($^{mineral/liquid}D$) are ≤0.1 for most incompatible elements, ≈1 for Eu and ≈10 for Ba and Sr [*Morra et al.*, 2003; *Bedard*, 2006; V. Morra, personal communication, 2006]. On this ground, the observed chemical variations within the MTN sample suite are consistent with crystallization (up to 40%) of prevalent sodic feldspar from microlite-poor, putative parental melts with geochemical signatures similar to those of AMS glasses, in agreement with textural data. In contrast, Ba, Sr and REE signatures of AMS glasses indicate that these latter represent residual melts which formed from their more primitive parental melts by minor (10–15%) fractional crystallization of feldspar phenocrysts and which, later on, were not significantly modified by further crystallization of feldspar microlites.

5.4. Volatiles and Water Exsolution Regime

[54] The measured in situ (SIMS-derived) residual water content variation ($H_2O = 0.21 \pm 0.05$ to 1.41 ± 0.82 wt%; Table 4) is not expected to be influenced by the other volatiles content as the H_2O solubility decreases for Cl >1.9 wt% [*Webster et al.*, 1999] and the analyzed glass does not

contain CO_2. Instead, a relationship between the in situ residual water content and groundmass texture exists for the investigated samples. Microlite-rich and vesicle-poor scoriae have a homogeneous residual water content of 0.21 ± 0.05 wt% (Table 4). Microlite-poor and vesicle-rich yellow microvesicular pumices are characterized by a heterogeneous residual water content with values up to 1.41 ± 0.82 wt% (Table 4). These data strongly suggest that the residual water content of the investigated CF magmas was controlled by the syneruptive magma dynamics. Both the general decrease in the volatiles content (Table 4 and Figure 6) and the heterogeneous textures displayed by our rocks, point to magma degassing as the main mechanism occurring during the eruptions. In the following, we will provide a discussion on the style of degassing taking into account only water, as it is the most abundant volatile in our samples and its content in CF products is available from the literature.

[55] The water content of CI, AMS and MTN magmas in the storage reservoir can be derived from recent studies on melt inclusions in phenocrysts [*Papale and Gresta*, 2006; M. Rutherford, personal communication, 2007]. Melt inclusions in CI pyroxenes exhibit up to 2.8 wt% of H_2O and <50 ppm of CO_2 [*Papale and Gresta*, 2006]. Melt inclusions in AMS pyroxenes and alkali-feldspars have water and carbon dioxide contents with values reaching 3.2 wt% and up to hundreds of ppm (generally below 50 ppm and subordinately up to ~200 ppm), respectively [*Papale and Gresta*, 2006]. Melt inclusions in the MTN phenocrysts show 2.2–3.8 wt% of water content and CO_2 below the detected limit (50 ppm) (M. Rutherford, personal communication, 2007). Overall, these studies indicate comparable water contents in the MTN, AMS and CI crystallizing magma chamber(s) and suggest an average pre-eruptive water content for CF magmas of about 3–4 wt%. A similar value for CI magmas has been also reported in previous studies of melt inclusions [*Signorelli et al.*, 2001; *Marianelli et al.*, 2002, 2006; *Webster et al.*, 2004] and phase equilibria [*Fowler et al.*, 2007]. This value has been also assumed in numerical simulation studies of the CF eruption dynamics [see, e.g., *Esposti Ongaro et al.*, 2006; *Todesco et al.*, 2006].

[56] Comparing the residual water content of the matrices with the pre-eruptive one derived from the literature, it can be suggested that the amount of water exsolved from the magma is higher for the

AMS and CI products and MTN scoriae than for the MTN pumice types. In particular, calculations based on the bulk residual water content allow us to infer that the exsolved water is $\sim$75–85% for the AMS and CI products and MTN scoriae, and $\leq$42–23% for the MTN pumice types. The different amounts of exsolved water obtained for our samples, associated with the overall data set discussed in the previous sections, suggests that two distinct mechanisms of degassing drove magma dynamics in the studied eruptions.

[57] An open-system degassing mechanism, possibly associated with low decompression rates, is able to explain the quiet escape of a volatile (H_2O) from the magma body and virtually contemporaneous melt crystallization. In agreement with observations on microlite and vesicle texture, and the homogeneous low residual water content, we suggest that open-system degassing was efficiently operating for the MTN eruption phase that discharged the scoriae. Assuming that the exsolution of H_2O occurred in equilibrium conditions, it is estimated that magma last equilibrated before fragmentation at a pressure <10 MPa [*Di Matteo et al.*, 2004]. On the other hand, closed-system degassing associated with a faster decompression rate determines the production of microlite-free or -poor pumice clasts, as those from the AMS and CI eruptions. The rapidity of the eruption process possibly favored degassing under disequilibrium conditions owing to prolonged high melt-vapor surface tension induced by the delayed vesicle formation and expansion [*Gardner and Denis*, 2004].

5.5. Magma Rheology as Deduced by Groundmass Texture and Composition

[58] The different intensity and magnitude of the three studied eruptions is not associated with significant differences in magma viscosity within the storage system. In fact, a similar pre-eruptive water content, temperature and composition as derived from petrological (see section 4) investigations, point to nearly identical viscosity for the MTN and CI magmas in pre-eruptive conditions (Figure 8a). Furthermore, these viscosities are up to one order of magnitude higher than those calculated for the AMS magma at the estimated eruptive temperatures. Our results indicate (see section 4.7) that viscosity strongly changes during crystallization and water exsolution (Figure 8c). For example, due to their different residual water contents (that implies

exsolution of different amounts of water from the three distinct erupted magmas), viscosity increases up to 1.5 log unit Pa s from MTN (H_2O $\sim$3–2 wt%, Table 4) to CI (H_2O $\sim$0.3–0.6 wt%, Table 4) and AMS (H_2O $\sim$0.7 wt%, Table 4) pumice clasts. Furthermore, the highest viscosity value is reached in water-poor (H_2O = 0.6 wt%, Table 4) and microlite-rich (26–32%, Table 1) scoriae from MTN (i.e., in products representing a more strongly degassed and crystallized melt), where viscosity is 2 log unit Pa s higher than that of the water-richer (H_2O = 3 wt%, Table 4) and microlite-poorer (1%, Table 1) basal MTN microvesicular pumice clasts. These differences in the viscosity values are known to affect the eruptive style [e.g., *Polacci et al.*, 2004], particularly when associated with variable timescales over which fluid dynamical properties change, as is the case with variations in the magma ascent (decompression) rate. A parametric study based on the produced data is beyond the scope of the present work and should be the subject of future research focused on a full comprehensive modeling of the eruption dynamics at CF.

6. Concluding Remarks

[59] We analyzed the textural and chemical characteristics of trachytic volcanic products generated at CF during three eruptions that strongly differ in terms of magnitude, intensity and eruptive style. By integrating our results with the literature data, we provide new insights into the dynamics of volatile exsolution and outgassing that are likely to occur during magma ascent along the volcanic conduit, in the course of explosive eruptions.

[60] In agreement with previous studies [e.g., *Eichelberger et al.*, 1986; *Jaupart and Allegre*, 1991; *Burgisser and Gardner*, 2005; *Gonnermann and Manga*, 2007], our textural and compositional data set suggests that, without important differences in the pre-eruptive magma composition and water content, the decompression rate (magma ascent rate) is the key parameter in driving changes in magma degassing style, rheology and explosivity of eruptions at CF. Ultimately, this conclusion leads to the more fundamental question of which factors affect the decompression rate. Below, we propose reliable mechanisms that should be deeply addressed in future studies.

[61] We propose that the low decompression (ascent) rate that determined the lower magnitude

phase of the MTN eruption (and related lowermost pumice deposits) may derive from early fragmentation caused by magma-water interaction during magma ascent. This hypothesis is supported by (1) the lithological features of the deposits along the stratigraphy [*D'Oriano et al.*, 2005]; (2) the lower amount of exsolved water (see section 5.4) and (3) the existence of quenching cracks in the glassy groundmass of pumice clasts (Figure 2). On the other hand, a rapid decompression (ascent) rate can be the result of a magma chamber recharge. Volcanological and petrological data [*de Vita et al.*, 1999; *Civetta et al.*, 1997] support this possibility for the AMS eruption. If no external water interacts with the rising magma and no magma chamber supply occurs, changes in the magma ascent rate may be triggered by (1) the dynamics of roof-rock fracturing and volcanic conduit formation and/or (2) the geometry of the magma chamber. Although there is an obvious correlation between the eruptions explosivity and the volume of the produced volcanic rocks, the lack of knowledge of the volume of magma available in the chamber before the eruption, at the present, precludes the possibility to make inferences on this topic.

Appendix A: Analytical Methods

A1. Scanning Electron Microscopy and 2-D Texture Quantification

[62] High-magnification Backscattered Electron (BSE) images were obtained using a ZEISS SU-PRA 35 at the "Dipartimento di Ingegneria dell'Informazione" of the II Università di Napoli in Aversa, Italy, operating at 10 keV and 7–12 mm work distance. Other BSE images were acquired using a LEO 430 SEM at the "Istituto Geomare Sud–CNR" of Napoli, Italy, operating at 10 keV and 15 mm work distance. The investigated areas vary from 0.2 to 5.4 mm^2. The resolution of the BSE images is 1 μm per pixel. BSE images were digitalized and processed (via the Adobe Photoshop® and NIH Image® software packages) to obtain 2-D data (numbers and areas) on groundmass vesicles and microlites. The following parameters were acquired: (1) the 2-D area fraction of vesicles and microlites and (2) the number densities of groundmass vesicles and microlites, i.e., the number of vesicles and microlites per unit area. Details of the procedure are given by *Piochi et al.* [2005b]. The analytical uncertainty on vesicularity

and crystallinity was about 5% and 10–20%, respectively.

A2. X-Ray Microtomography and 3-D Texture Quantification

[63] X-ray computed microtomography is the only high-resolution, nondestructive technique that allows reconstruction and quantification of the internal structure of porous materials directly in three dimensions, revealing textural features that are not unambiguously recognized via solely 2-D thin section investigation. Tomographic experiments were conducted at the SYRMEP beamline of the Elettra Sincrotrone facility in Basovizza (Italy); the following conditions were applied to all the investigated samples: 2.4 GeV beam energy, 17 to 25 keV ring energy, 7.88 × 7.88 mm^2 CCD field of view, 3.85 μm pixel size (see *Polacci et al.* [2006] for details on the procedure). The obtained 2-D image slices were stacked and processed via the ImageJ® software package to produce a 3-D digital view of each sample. Vesicles were separated and counted with the Blob3D software package [*Ketcham*, 2005], following segmentation upon simple grey-scale thresholding. Quantification of 3-D vesicle textures included measurements of vesicularity (volumetric fraction of vesicles), number densities (number of vesicles per unit volume) and % of interconnectivity (reported as volume fraction of connected vesicles/volume fraction of total vesicles). The analytical uncertainty on vesicularity using this procedure is estimated to be <5%.

A3. Electron and Ion Microprobe Analyses

[64] Major-element analyses of glass and microlites were obtained from polished thin sections using a Cameca SX-50 Electron Microprobe at the "Istituto di Geologia Ambientale e Geoingegneria" (CNR), in Roma, Italy. The following operating conditions for WDS (Wavelength Dispersive Spectroscopy) analysis have been adopted: 10 nA beam current, 15 keV accelerating voltage and 100 sec counting time. For each spot analysis, alkalis were always concurrently counted during the first 15 sec, using a defocused beam size of 10 μm, in order to limit the degree of volatilization during probing. This beam size was adopted also for glass analyses; otherwise, the beam size was 5 μm. Data reduction was made using the ZAF4/FLS software by Link Analytical. Detection limit at 3σ above mean background was generally <200 ppm for the analyzed elements. The uncertainty is of ~1% for most major elements, between 1 to 3% for

alkalis, and up to 10% for elements at concentration levels <0.2 wt%.

[65] Volatile (H, F and Cl) elements were analyzed by Secondary Ion Mass Spectrometry (SIMS) using a Cameca IMS4f installed at Istituto di Geoscienze e Georisorse (CNR-IGG), Pavia, Italy. The primary ion beam consisted of mass-filtered $^{16}O^-$, which was focused on 15–20 μm diameter spots, typically at a primary current intensity of 10 nA. The primary accelerating voltage was 12.5 kV. The secondary ions sputtered from polished and platinum-coated samples were transferred to the mass spectrometer using a nominal accelerating voltage of 4.5 kV, with an ion-imaged field of 25-μm diameter. To minimize both molecular interference and matrix effects, the "Conventional Energy Filtering" technique (CEF) was applied by offsetting the accelerating voltage of 100 V, while keeping a constant voltage for the electrostatic analyzer, as well as constant settings for the width and position of the energy slit. The latter was symmetrically opened to a width of 50 eV, thus enabling the analysis of secondary ions with emission kinetic energies ranging from 75 to 125 eV. Data reduction was carried out according to the procedures described by *Ottolini et al.* [1993, 1995] and *Tiepolo et al.* [2005] using relative-to-Si ion yields assessed by repeated analysis of natural minerals, and both natural and synthetic glasses. Precision and accuracy for H_2O contents >0.1 wt%, as well as for the Cl and F determination, were estimated to be better than 10% and 15%, respectively.

A4. Laser Ablation Microprobe Analyses

[66] In situ analyses of REE, LILLE, HFSE and other relevant trace elements were carried out using Laser-Ablation Inductively Coupled-Plasma Mass-Spectrometry at CNR-IGG, Pavia, Italy. The laser probe consists of a Q-switched Nd:YAG laser, model Quantel (Brilliant), whose fundamental emission in the near-IR region (1064 nm) was converted to either 266 nm or 213 nm wavelengths. The spot diameter was typically 20–50 μm. The ablated material was analyzed using an Elan DRC-e (Perkin Elmer) quadrupole mass spectrometer. Helium was used as carrier gas and mixed with Ar downstream of the ablation cell. NIST SRM 610 was used as external standard. Si was used as internal standard. Precision and accuracy were assessed from repeated analyses of the BCR-2g or NIST SRM

612 standards and both resulted better than 10%. A detailed description of instrumental parameters and quantification procedure is given by *Tiepolo et al.* [2003]. Ablation time varied from tens of seconds to very few seconds.

A5 Vesicle-Free Glass Preparation

[67] Pumice and scoria clasts were cleaned with distilled water and crushed, and the grain size fractions <1Φ were separated by sieving. Whenever possible, phenocrysts were removed by handpicking under a binocular microscope. The efficiency in removing phenocrysts from the samples ranged between 90% and 80%, depending on the different porphyricity index and texture (see section 4.1). Aliquots of the phenocryst-free fractions were powdered and heated at 100°C in a furnace for at least 10 hours. Then they were melted in sealed gold–palladium capsules at 5 kbar and 1100°C for 45 min and rapidly quenched under an uniaxial hydraulic press in the high-pressure laboratory of the Istituto Nazionale di Geofisica e Vulcanologia (Roma, Italy). Because phenocryst cleaning in the samples was not entirely efficient, we take into account the likely presence of hydrous and melt-inclusions-bearing crystals with size <1Φ and estimate that the measured water content could be overestimated by about 20–25%.

A6. FT-IR Analyses

[68] FT-IR analyses were carried out at the laboratory of the Istituto Nazionale di Geofisica e Vulcanologia, Osservatorio Vesuviano, Napoli, Italy, by using a Nicolet Nexus spectrometer equipped with a Continuum microscope. A globar source, KBr beam splitter and a-nitrogen cooled MCT/A detector over mid-IR range (650–6000 cm^{-1}) and 1000 scans allowed us the collection of the transmittance spectra. Resolution was 4 cm^{-1}. Three spots were analyzed for each sample. H_2O concentrations were calculated using the absorbance for bands at 5200 (molecular) and 4500 (OH$^-$ group) cm^{-1}. No peaks were detected at 1565 cm^{-1}. The absorbance of a given band (abs) is related to the species concentration (c in weight fraction) by the *Newman et al.* [1986] equation:

$$c = (MW)(abs)/(\rho d\alpha)$$

where MW is the molecular weight of H_2O (g mol^{-1}), ρ the density of the glass (2.2 to 2.5 g/cm^3), d the

Table B1. Outcrop Location

Stratigraphic Unit	Sample	Location	Latitude N	Longitude E
Campanian Ignimbrite	IC 60–90	Voscone	40°48′00–47′50	14°38′42–39′20
Agnano Monte Spina	AMS B1, AMS D1, FL1c, FL1a	Camaldoli, Il Castagno	40°51′33	14°12′03
Monte Nuovo LM	LM inf, LM inb	Lucrino, Tripergole	40°49′55–56	14°05′25–27
Monte Nuovo LM	MN1/1	Lucrino, Tripergole	40°49′52	14°05′26–29
Monte Nuovo LM	LM c1, LM c2, LM c3, MN 2/3, MN 2/1	Arco Felice, Oasi	40°49′57–58	14°05′17–21
Monte Nuovo UM	UM1, MN4 top, MN4/1	Arco Felice, Oasi	40°49′57–58	14°05′17–21

thickness (76 to 190 μm) and α the molar absorptivity (L mol^{-1} cm^{-1}) (1.25, 1.10 at 5200, 4500 cm^{-1}, respectively [*Carroll and Blank*, 1997]).

Appendix B: Outcrop Locations

[69] The CI, AMS, and MTN rocks, which represent the products of eruptions with very high, high and low intensity and magnitude, respectively, have been sampled in localities well-known in the current literature: (1) CI at Voscone [*Rosi et al.*, 1999]; (2) AMS at Camaldoli [*de Vita et al.*, 1999] and (3) MTN at Monte Nuovo [*D'Oriano et al.*, 2005; *Piochi et al.*, 2005b]. Therefore, the cited papers provide the basic petrological and volcanological information on the samples investigated in this study. Table B1 shows details of the outcrop locations.

References

Alidibirov, M. A., and D. B. Dingwell (1996), An experimental facility for investigation of magma fragmentation by rapid decompression, *Bull. Volcanol.*, *58*, 411–416.

Alidibirov, M. A., and D. B. Dingwell (2000), Three fragmentation mechanisms for highly viscous magma under rapid decompression, *J. Volcanol. Geotherm. Res.*, *100*, 413–421.

Barberi, F., G. Corrado, F. Innocenti, and G. Luongo (1984), Phlegraean Fields 1982–1984: Brief chronicle of a volcano emergency in a densely populated area, *Bull. Volcanol.*, *47*(2), 175–185.

Bedard, J. H. (2006), Trace element partitioning in plagioclase feldspar, *Geochim. Cosmochim. Acta*, *70*, 3717–3742.

Burgisser, A., and J. E. Gardner (2005), Experimental constraints on degassing and permeability in volcanic conduit flow, *Bull. Volcanol.*, *67*, 42–56, doi:10.1007/s00445-004-0359-5.

Caricchi, L., L. Burlini, P. Ulmer, T. Gerya, M. Vassalli, and P. Papale (2007), Non-Newtonian rheology of crystal-bearing magmas and implications for magma ascent dynamics, *Earth Planet. Sci. Lett.*, *264*(3–4), 402–419.

Carroll, M. R., and J. Blank (1997), Solubility of water in phonolitic melts, *Am. Mineral.*, *82*, 1111–1115.

Cashman, K. V., and J. D. Blundy (2000), Degassing and crystallization of ascending andesite and dacite, *Philos. Trans. R. Soc. London, Ser. A*, *358*, 1487–1513.

Cashman, K. V., B. Sturtenvant, P. Papale, and O. Navon (2000), Magmatic fragmentation, in *Encyclopedia of Volcanoes*, edited by H. Sigurdsson et al., pp. 421–430, Academic, San Diego, Calif.

Chiodini, G., C. Cardellini, F. Frondini, D. Granieri, L. Marini, and G. Ventura (2001), CO_2 degassing and energy release at Solfatara Volcano, Campi Flegrei, Italy, *J. Geophys. Res.*, *106*(B8), 16,213–16,221.

Civetta, L., G. Orsi, L. Pappalardo, R. V. Fisher, G. Heiken, and M. Ort (1997), Geochemical zoning, mingling, eruptive dynamics and depositional processes—The Campanian Ignimbrite, Campi Flegrei caldera, Italy, *J. Volcanol. Geotherm. Res.*, *75*, 183–219.

Costa, A., O. Melnik, R. S. J. Sparks, and B. Voight (2007), Control of magma flow in dykes on cyclic lava dome extrusion, *Geophys. Res. Lett.*, *34*, L02303, doi:10.1029/2006GL027466.

Couch, S., R. S. J. Sparks, and M. R. Carroll (2003), The kinetics of degassing-induced crystallization at Soufriere Hills Volcano, Montserrat, *J. Petrol.*, *44*, 1477–1502.

D'Antonio, M., L. Civetta, G. Orsi, L. Pappalardo, M. Piochi, A. Carandente, S. de Vita, M. Di Vito, and R. Isaia (1999), The present state of the magmatic system of the Campi Flegrei caldera based on a reconstruction of its behavior in the past 12 ka, *J. Volcanol. Geotherm. Res.*, *91*, 247–268.

Deino, A. L., G. Orsi, S. de Vita, and M. Piochi (2004), The age of the Neapolitan Yellow Tuff caldera-forming eruption (Campi Flegrei caldera–Italy) assessed by $^{40}Ar/^{39}Ar$ dating method, *J. Volcanol. Geotherm. Res.*, *133*, 157–170.

Dellino, P., R. Isaia, L. La Volpe, and G. Orsi (2001), Statistical analysis of textural data from complex pyroclastic sequences: Implications for fragmentation processes of the Agnano-Monte Spina tephra (4.1 ka), Phlegraean Fields, southern Italy, *Bull. Volcanol.*, *63*, 443–461.

de Vita, S. (1999), et al The Agnano-Monte Spina eruption (4100 years BP) in the restless Campi Flegrei caldera (Italy), *J. Volcanol. Geotherm. Res.*, *91*, 269–301.

De Vivo, B., G. Rolandi, P. B. Gans, A. Calvert, W. A. Bohrson, F. J. Spera, and H. E. Belkin (2001), New constraints on the pyroclastic eruptive history of the Campanian volcanic Plain (Italy), *Mineral. Petrol.*, *73*, 47–65.

Di Matteo, V., M. R. Carroll, H. Behrens, F. Vetere, and R. A. Brooker (2004), Water solubility in trachytic melts, *Chem. Geol.*, *213*, 187–196.

Di Vito, M. A., L. Lirer, G. Mastrolorenzo, and G. Rolandi (1987), The Monte Nuovo eruption (Campi Flegrei, Italy), *Bull. Volcanol.*, *49*, 608–615.

Di Vito, M. A., R. Isaia, G. Orsi, J. Southon, M. D'Antonio, S. de Vita, L. Pappalardo, and M. Piochi (1999), Volcanic and deformation history of the Campi Flegrei caldera in the past 12 ka, *J. Volcanol. Geotherm. Res.*, *91*(2–4), 221–246.

D'Oriano, C., E. Poggianti, A. Bertagnini, R. Cioni, P. Landi, M. Polacci, and M. Rosi (2005), Changes in eruptive style during the A.D. 1538 Monte Nuovo eruption (Phlegrean Fields, Italy): The role of syn-eruptive crystallization, *Bull. Volcanol.*, *67*, 601–621, doi:10.1007/s00445-004-0397-z.

Eichelberger, J. C., C. R. Carrigan, H. R. Westrich, and R. H. Price (1986), Nonexplosive silicic volcanism, *Nature*, *323*, 598–602.

Elkins, L., and T. Grove (1990), Ternary feldspar experiments and thermodynamic models, *Am. Mineral.*, *45*(5–6), 544–559.

Esposti Ongaro, T., P. Papale, A. Neri, and D. Del Seppia (2006), Influence of carbon dioxide on the large-scale dynamics of magmatic eruptions at Phlegrean Fields (Italy), *Geophys. Res. Lett.*, *33*, L06318, doi:10.1029/2005GL025528.

Fisher, R. V., G. Orsi, M. Ort, and G. Heiken (1993), Mobility of a large volume pyroclastic flow—Emplacement of the Campanian ignimbrite, Italy, *J. Volcanol. Geotherm. Res.*, *56*, 205–220.

Fowler, S. J., F. J. Spera, W. A. Bohrson, H. E. Belkin, and B. De Vivo (2007), Phase equilibria constraints on the chemical and physical evolution of the Campanian ignimbrite, *J. Petrol.*, *48*, 459–493.

Gardner, J. E., and M. Denis (2004), Heterogeneous bubble nucleation on Fe-Ti oxide crystals in high-silica rhyolitic melts, *Geochim. Cosmochim. Acta*, *68*, 3587–3597.

Gerlach, M. T., H. R. Westrich, and R. B. Symonds (1996), Pre-eruption vapor in magma of the climactic Mount Pinatubo eruption: Source of the giant stratospheric sulfur dioxide cloud, in *Fire and Mud: Eruptions and Lahars of Mount Pinatubo, Philippines*, edited by C. G. Newhall and R. S. Punongbayan, pp. 415–433, Univ. of Wash. Press, Seattle, Wash.

Geschwind, C. H., and M. J. Rutherford (1995), Crystallization of microlites during magma ascent: The fluid mechanism of 1980–1986 eruption at Mount St Helens, *Bull. Volcanol.*, *57*, 356–370.

Giordano, D., C. Romano, P. Papale, and D. B. Dingwell (2004), The viscosity of trachytes, and comparison with basalts, phonolites, and rhyolites, *Chem. Geol.*, *213*, 49–61.

Giordano, D., J. K. Russell, and D. B. Dingwell (2008), Viscosity of natural silicate melts: A model, *Earth Planet. Sci. Lett*, in press.

Gonnermann, H. M., and M. Manga (2007), The fluid mechanics inside a volcano, *Annu. Rev. Fluid Mech.*, *39*, 321–356.

Housh, T. B., and J. F. Luhr (1991), Plagioclase-melt equilibria in hydrous systems *Am. Mineral.*, *76*, 477–492.

Issel, A. (1883), Le oscillazioni lente del suolo o bradisismi, *Atti Regia Univ. Genova*, *IV*, pp. 1–210, Genova, Italy.

Jaupart, C., and C. Allegre (1991), Gas content, eruption rate and instabilities of eruption regime in silicic volcanoes, *Earth Planet. Sci. Lett.*, *102*, 413–429.

Ketcham, R. A. (2005), Computational methods for quantitative analysis of three-dimensional features in geological specimens, *Geosphere*, *1*, 32–41.

Le Bas, M. J., R. W. Le Maitre, A. Streckeisen, and B. Zanettin (1986), A chemical classification of volcanic rocks based on the total alkali-silica diagram, *J. Petrol.*, *27*, 745–750.

Lirer, L., G. Rolandi, M. A. Di Vito, and G. Mastrolorenzo (1987), L'eruzione del Monte Nuovo (1538) nei Campi Flegrei, *Boll. Soc. Geol. It.*, *106*, 447–460.

Mangan, M. T., and T. W. Sisson (2000), Delayed, disequilibrium degassing in rhyolite magma: Decompression experiments and implications for explosive volcanism, *Earth Planet. Sci. Lett.*, *183*, 441–455.

Marianelli, P., M. Proto, and A. Sbrana (2002), The Ignimbrite Campana magma chamber: Pre-eruptive P-T-X conditions from melt inclusion data (abstract), paper presented at EGS-AGU-EUG Joint Assembly, Eur. Geophys. Soc., Nice, France, 21 –26 April .

Marianelli, P., A. Sbrana, and M. Proto (2006), Magma chamber of the Campi Flegrei supervolcano at the time of eruption of the Campanian Ignimbrite, *Geology*, *34*, 937–940, doi:10.1130/G22807A.1.

Morra, V., M. Lustrino, L. Melluso, G. Ricci, R. Vannucci, A. Zanetti, and F. D'Amelio (2003), Trace element partition coefficients between feldspar, clinopyroxene, biotite, Ti-magnetite, apatite and felsic potassic glass from Campi Flegrei (S. Italy) (abstract), paper presented at EGS-AGU-EUG Joint Assembly, Eur. Geophys. Soc., Nice, France, 6–11 April.

Newman, S., E. M. Stopler, and S. Epstein (1986), Measurement of water in rhyolitic glasses: Calibration of an infrared spectroscopic technique, *Am. Mineral.*, *71*, 1527–1541.

Orsi, G., S. de Vita, and M. A. Di Vito (1996), The restless, resurgent Campi Flegrei nested caldera (Italy): Constraints on its evolution and configuration, *J. Volcanol. Geotherm. Res.*, *74*, 179–214.

Orsi, G., C. Del Gaudio, S. de Vita, M. A. Di Vito, S. M. Petrazzuoli, G. Ricciardi, and C. Ricco (1999), Short-term ground deformations and seismicity in the nested Campi Flegrei caldera (Italy): An example of active block resurgent in a densely populated area, *J. Volcanol. Geotherm. Res.*, *91*, 415–451.

Ottolini, L., P. Bottazzi, and R. Vannucci (1993), Quantification of lithium, beryllium and boron in silicates by secondary ion mass spectrometry using conventional energy filtering, *Anal. Chem.*, *65*, 1960–1968.

Ottolini, L., P. Bottazzi, A. Zanetti, and R. Vannucci (1995), Determination of hydrogen in silicates by Secondary Ion Mass Spectrometry, *Analyst*, *120*, 1309–1314.

Papale, P., and S. Gresta (2006), The Campi Flegrei, Proceedings of the meeting "Frame programme for the meeting and Research Activity on Italian Volcanoes 2005–2007," report, *INGV-DPC Proj. V3_2*, 129 pp., Dip. per la Protezione Civile and Ist. Naz. di Geofis. e Vulcanol., Rome.

Papale, P., and M. Polacci (1999), Role of carbon dioxide in the dynamics of magma ascent in explosive eruptions, *Bull. Volcanol.*, *60*, 583–594.

Pappalardo, L. (1994), Chemostratigrafia dei prodotti dell'Ignimbrite Campana in area distale, Ph.D. thesis, 150 pp., Univ. of Napoli, Napoli, Italy.

Pappalardo, L., M. Piochi, M. D'Antonio, L. Civetta, and R. Petrini (2002), Evidence for multi-stage magmatic evolution during the past 60 ka at Campi Flegrei (Italy) deduced from Sr, Nd and Pb isotope data, *J. Petrol.*, *43*(7), 1415–1434.

Piochi, M., P. P. Bruno, and G. De Astis (2005a), Relative roles of rifting tectonics and magma ascent processes: Inferences from geophysical, structural, volcanological, and geochemical data for the Neapolitan volcanic region (southern Italy), *Geochem. Geophys. Geosyst.*, *6*, Q07005, doi:10.1029/2004GC000885.

Piochi, M., G. Mastrolorenzo, and L. Pappalardo (2005b), Magma ascent and eruptive processes from textural and compositional features of Monte Nuovo pyroclastic products, Campi Flegrei, Italy, *Bull. Volcanol.*, *67*, 663–678, doi:10.1007/s00445-005-0410-1.

Polacci, M. (2005), Constraining the dynamics of volcanic eruptions by characterization of pumice textures, *Ann. Geophys.*, *48*, 731–738.

Polacci, M., L. Pioli, and M. Rosi (2003), The Plinian phase of the Campanian Ignimbrite eruption (Phlegrean Fields, Italy): Evidence from density measurements and textural characterization of pumice, *Bull. Volcanol.*, *65*, 418–432.

Polacci, M., P. Papale, D. Del Seppia, D. Giordano, and C. Romano (2004), Dynamics of magma ascent and fragmentation in trachytic versus rhyolitic eruptions, *J. Volcanol. Geotherm. Res.*, *131*, 93–108.

Polacci, M., D. R. Baker, L. Mancini, G. Tromba, and F. Zanini (2006), Three-dimensional investigation of volcanic textures by X-ray microtomography and implications for conduit processes, *Geophys. Res. Lett.*, *33*, L13312, doi:10.1029/2006GL026241.

Proussevitch, A. A., D. L. Sahagian, and A. T. Anderson (1993), Dynamics of diffusive bubble growth in magmas: Isothermal case, *J. Geophys. Res.*, *98*, 22,283–22,307.

Romano, C., D. Giordano, P. Papale, V. Mincione, D. Dingwell, and M. Rosi (2003), The dry and hydrous viscosities of alkaline melts from Vesuvius and Phlegrean Fields, *Chem. Geol.*, *202*, 23–38.

Rosi, M., and R. Santacroce (1984), Volcanic hazard assessment in the Phlegrean Fields: A contribution based on stratigraphic and historical data, *Bull. Volcanol.*, *47*(2), 359–370.

Rosi, M., and A. Sbrana (1987), The Phlegraean Fields, Quaderni de "La Ricerca Scientifica,"175 pp., Cons. Naz. delle Ric., Rome.

Rosi, M., L. Vezzoli, A. Castelmenzano, and G. Grieco (1999), Plinian pumice fall deposit of the Campanian Ignimbrite eruption (Phlegraean Fields, Italy), *J. Volcanol. Geotherm. Res.*, *91*, 179–198.

Shaoxiong, W., and H. Nekvasil (1994), SOLVCALC: An interactive graphic program package for calculating the ternary feldspar solvus and for two feldspars geothermometry, *Comput. Geosci.*, *20*, 1025–1040.

Signorelli, S., G. Vaggelli, C. Romano, and M. R. Carroll (2001), Volatile element zonation in Campanian Ignimbrite magmas (Phlegrean Fields, Italy): Evidence from the study of glass inclusions and matrix glasses, *Contrib. Mineral. Petrol.*, *140*, 543–553.

Sparks, R. S. J. (1978), The dynamics of bubble formation and growth in magmas: A review and new analysis, *J. Volcanol. Geotherm. Res.*, *3*, 1–37.

Spieler, O., B. Kennedy, U. Kueppers, D. B. Dingwell, B. Scheu, and J. Taddeucci (2004), The fragmentation threshold of pyroclastic rocks, *Earth Planet. Sc. Lett.*, *226*, 139–148.

Sun, S., and W. F. McDonough (1989), Chemical and isotopic systematics of oceanic basalts: Implications for mantle composition and processes, in *Magmatism in the Ocean Basins*, edited by A. D. Saunders and M. J. Norry, *Geol. Soc. Spec. Publ.*, *42*, 313–346.

Tiepolo, M., P. Bottazzi, M. Palenzona, and R. Vannucci (2003), A laser probe coupled with ICP–double-focusing sector-field mass spectrometer for in situ analysis of geological samples and U-Pb dating of zircon, *Can. Mineral.*, *41*, 259–272.

Tiepolo, M., A. Zanetti, and R. Vannucci (2005), Determination of Li, Be and B at trace levels by LA-ICP-MS, *Geostand. Geoanal. Res.*, *29*, 211–224.

Todesco, M., A. Neri, T. Esposti Ongaro, P. Papale, and M. Rosi (2006), Pyroclastic flow dynamics and hazard in a caldera setting: Application to Phlegrean Fields (Italy), *Geochem. Geophys. Geosyst.*, *7*, Q11003, doi:10.1029/2006GC001314.

Webster, J. D., R. J. Kinzler, and E. A. Mathez (1999), Chloride and water solubility in basalt and andesite melts and implications for magmatic degassing, *Geochim. Cosmochim. Acta*, *63*(5), 729–738.

Webster, J. D., F. Raia, C. Tappen, and B. De Vivo (2004), Preeruptive geochemistry of the ignimbrite-forming magmas of the Campanian Volcanic Zone, southern Italy, determined from silicate melt inclusions, *Mineral. Petrol.*, *79*, 99–125, doi:10.1007/s00710-003-0004-6.